Conformational dynamics and asymmetry in multimodal inhibition of membrane-bound pyrophosphatases

Jianing Liu[1^], Anokhi Shah[2,3^], Yue Ma[2,3], Katie Hardman[4], Niklas G. Johansson[5], Orquidea Ribeiro[1], Adam Brookfield[6], Alice Bowen[6], Jari Yli-Kauhaluoma[5], Henri Xhaard[5], Lars J.C. Jeuken[7], Adrian Goldman[1*], Christos Pliotas[2,3*], Keni Vidilaseris[1*]

[1]Research Program in Molecular and Integrative Biosciences, University of Helsinki, Helsinki, Finland

[2]BioEmPiRe Centre for Structural Biological EPR Spectroscopy, School of Biological Sciences, Faculty of Biology, Medicine and Health, University of Manchester, Manchester M13 9PT, UK

[3]Manchester Institute of Biotechnology, University of Manchester, Manchester M1 7DN, UK

[4]Astbury Centre for Structural Molecular Biology, School of Biomedical Sciences, University of Leeds, Leeds LS2 9JT, UK

[5]Drug Research Program, Division of Pharmaceutical Chemistry and Technology, Faculty of Pharmacy, University of Helsinki, Helsinki, Finland

[6]The National Research Facility for Electron Paramagnetic Resonance, The Photon Science Institute and The Department of Chemistry, University of Manchester, Manchester, M13 9PL, UK

[7]Leiden Institute of Chemistry, University Leiden, PO Box 9502, 2300 RA Leiden, The Netherlands.

[^]Joint first author

[*]Corresponding authors:

Adrian Goldman (adrian.goldman@helsinki.fi)

Christos Pliotas (christos.pliotas@manchester.ac.uk)

Keni Vidilaseris (keni.vidilaseris@helsinki.fi)

Running title: Conformational dynamics of membrane-bound pyrophosphatases

Keywords: Bisphosphonates / DEER / PELDOR / EPR spectroscopy / Membrane-bound pyrophosphatase / X-ray crystallography

Abstract

Membrane-bound pyrophosphatases (mPPases) are homodimeric proteins that hydrolyse pyrophosphate and pump H^+/Na^+ across membranes. They are crucial for the virulence of protist pathogens, making them attractive drug targets. In this study, we investigate the inhibitory effects of seven distinct bisphosphonates against *Thermotoga maritima* mPPase to explore their mode of action and assist in future small molecule inhibitor development. We solved two structures of mPPase bound to the inhibitors in the enzyme active sites and probed the conformational dynamics of mPPase under multiple inhibitors and functionally relevant conditions by double electron-electron resonance (DEER) spectroscopy. We found that mPPase adopts five distinct conformations within the ensemble in the presence of different inhibitors. Combined with solid-supported membrane-based electrophysiology recordings, this revealed that during catalysis, one monomer of the dimer remains open, and Na^+ can only be pumped in a closed state. These results further support the existence of catalytic asymmetry in our pumping-before-hydrolysis model.

Introduction

Membrane-bound pyrophosphatases (mPPases) facilitate the transport of protons and/or sodium ions across membranes while catalysing the breakdown of pyrophosphate (PP_i), a by-product generated in various cellular synthetic reactions - into inorganic phosphate (P_i). These enzymes are found in plants, certain species of bacteria, protist parasites, and archaea, but are absent from multicellular animals[1-5]. Within these organisms, mPPases are essential for cell survival under diverse stress conditions such as osmotic stress, mineral deficiency, and extreme temperature[6]. Based on their potassium dependency, mPPases are divided into two families: K^+-dependent and K^+-independent. While K^+-independent mPPases all transport H^+, K^+-dependent mPPases can transport H^+, Na^+, or both[4].

Currently, mPPase structures from three different organisms have been reported: *Vigna radiata (*VrPPase), *Thermotoga maritima* (TmPPase), and, most recently, a structure from *Pyrobaculum aerophilum* (PaPPase) in complex with imidodiphosphate (IDP)[7]. For TmPPase, several different structural states have been determined, including the resting state (TmPPase:Ca:Mg)[8], with two phosphates bound (TmPPase:2P_i)[8], IDP bound (TmPPase:IDP)[9], IDP and *N*-[(2-amino-6-benzothiazolyl)methyl]-1*H*-indole-2-carboxamide (ATC) bound (TmPPase:IDP:ATC)[10], phosphate analogue (WO_4)-bound (TmPPase:WO_4)[9], and time-resolved X-ray diffraction structures (with and without substrate/product bound) showing structural asymmetry[7]. Similarly, VrPPase has been solved in multiple states, including IDP-bound (VrPPase:IDP)[11], single phosphate-bound (VrPPase:P_i)[9], two phosphates bound (VrPPase:2P_i), and different mutations at the hydrophobic gate[12]. These structures show that mPPases are homodimeric enzymes, with each monomer consisting of 16 transmembrane helices (TMHs), occasionally 17 TMHs as found in the sequence databases, organised into two concentric rings: the inner ring (TMH5-6, 11-12, and 15-16) and the outer ring (TMH1-4, 7-10, and 13-14). Each monomer consists of four regions: a hydrolytic centre, a coupling funnel, an ion gate, and an exit channel[13] (Fig. 1A). To simplify residue comparison between mPPases, we employ the residue numbering scheme $X\Sigma^{Y.Z}$ (superscripts refer to Ballesteros–Weinstein numbering[14]), where X represents the amino acid, Σ denotes the amino acid position in TmPPase, Y indicates the helix number, and Z specifies the offset of amino acid positions within the centrally conserved residues of the helix[12,15].

mPPases are a promising drug target for treating diseases caused by parasitic protists, such as malaria and leishmaniasis[10,16-18]. Among the currently available compounds, ATC demonstrates the most effective inhibitory activity against TmPPase[20]. ATC is bound to a region near the enzyme exit channel of one subunit, which induces structural asymmetry in the mPPase dimer[20]. Functional asymmetry in K^+-dependent mPPases has also previously been shown by Artukka, et al. [21]. Anashkin and coworkers[22]

further supported this hypothesis by analysing the inhibition of *Desulfitobacterium hafniense* mPPase using three non-hydrolysable PP_i analogues (IDP, etidronate (ETD), and aminomethane bisphosphonate). Bisphosphonates, such as risedronate (RSD) and pamidronate (PMD), serve as primary drugs currently used to combat osteoclast-mediated bone loss[23]. Unlike IDP, which contains a P-N-P bond, bisphosphonates have a P-C-P bond, with its central carbon can accommodate up to two substituents, allowing a large compound variability. Therefore, understanding their inhibition mechanism on mPPases is crucial for developing future small molecule inhibitors.

Our previous work on serial time-resolved X-ray crystallography and electrometric studies on TmPPase showed a direct observation of structural asymmetry, where two monomers are in different states during PP_i hydrolysis upon the addition of substrate and Na^+, supporting a "pumping-before-hydrolysis" energy coupling model[7]. However, except for the allosteric inhibitor ATC, which binds to a region near the exit channel, crystal structures of TmPPase bound to inhibitors at the active site are symmetric. In order to probe the proposed asymmetry caused by the inhibitor (and substrate) binding in solution, we employed double electron-electron resonance (DEER), also known as pulsed electron double resonance (PELDOR) spectroscopy. This method relies on the introduction of spin labels on selected protein sites, allowing for precise determination of inter-spin distances[24-26], making it a powerful tool for probing the conformation and dynamics of integral membrane proteins[27-30], including ion channels, transporters, outer membrane proteins, and receptors in their native environments[31-37]. As an ensemble technique, DEER can probe the presence of multiple conformational species in solution including lowly populated protein states, which are key to the protein function[38-40]. Here, we solved two TmPPase structures in complex with ETD and zoledronate (ZLD) and monitored their conformational ensemble using DEER spectroscopy in solution. Overall, bisphosphonates can trigger conformational changes in the active site and near the exit channel of TmPPase in an asymmetric mode and under certain inhibitor-bound conditions, the DEER data correlate with the expected distances of an open/closed asymmetric model, consistent with the corresponding X-ray structures. This, along with our electrometric studies detecting the Na^+ signal across the membrane, further suggests that ion pumping requires a fully closed state of one TmPPase monomer, supporting our pumping-before-hydrolysis model[7].

Results

Bisphosphonates are weaker TmPPase inhibitors than IDP

Bisphosphonates have been shown to inhibit mPPases[22,41]. To understand their binding mechanism to TmPPase, we first assessed the binding ability of seven distinct bisphosphonates to TmPPase by testing their inhibitory activity using the molybdenum blue assay[42] (Fig. 1B), with IDP (IC_{50} = 56.4 $\pm$ 5.4 µM) as a positive control[19]. Of the compounds tested, all the straight-chain primary amines had similar IC_{50}s, ranging from 117 to 138 µM (*P* = 0.06). Substituting the -NH- of IDP with the $–CCH_3(OH)–$ of ETD resulted in a significantly weaker IC_{50} (> 200 µM). Similarly, branched aliphatic and aromatic bisphosphonates (ibandronate (IBD), ZLD and RSD) also showed weaker inhibition (IC_{50} > 200 µM) (Fig. 1B and Fig. EV1).

To confirm that the binding of bisphosphonates to TmPPase induces conformational changes in the protein structure, we incubated the enzyme with the inhibitors and performed an *N*-ethyl maleimide (NEM) modification assay[43]. NEM covalently binds to exposed cysteine residues of the protein, forming a carbon-sulfur bond that can inhibit the protein activity if the residue is essential[8]. IDP has been reported to prevent the NEM modification of cysteine by retaining TmPPase activity[8]. In the absence of inhibitors, NEM modification resulted in a decrease in TmPPase activity by approximately 40% (Fig. 1C), similar to the activity reduction observed with $CaCl_2$, an inhibitor that binds to the open form of TmPPase[8]. Upon the addition of IDP, TmPPase adopts a closed conformation, rendering it resistant to NEM modification[8] (Fig. EV2); consequently, the enzyme remains largely unaffected by NEM. Although not as effective as IDP, all bisphosphonates prevent NEM modification to a comparable extent (Fig. 1C).

TmPPase structures in complex with bisphosphonate inhibitors

To decipher the structural basis of bisphosphonates inhibition and their binding to TmPPase, we decided to solve their structures since all the bisphosphonates bound to TmPPase despite not being isosteres of PP_i (Fig. 1). We obtained protein crystals for all the inhibitors, but they diffracted weakly, except for TmPPase in complex with ETD (TmPPase:ETD) and ZLD (TmPPase:ZLD), which diffracted to resolutions of 3.2 Å and 3.3 Å, respectively. TmPPase:ETD crystallised in the presence of Ca^{2+}, which is a well-known mPPase inhibitor[8], while TmPPase:ZLD crystallised without Ca^{2+}. Both data sets were anisotropic as analysed using the STARANISO server[44] (Table S1). We solved both structures by molecular replacement using the resting state structure (PDB ID: 4AV3) as the search model for

TmPPase:ETD and the closed IDP-bound structure (PDB ID: 5LZQ) for TmPPase:ZLD. There were two molecules in the asymmetric unit for TmPPase:ETD and four for TmPPase:ZLD.

In the initial round of the refinement for the TmPPase:ETD structure, both chains displayed positive (F_o-F_c) density at 3σ in their hydrolytic centres that could accommodate ETD (Figs. EV3A-B, *upper left panel*). We also observed extra density that corresponds to a calcium ion in the resting state structure[8] (Figs. EV3A,B, *upper left panel*). Due to the high Ca^{2+} concentration (0.2 M) in the crystallisation condition, we placed the same ion at this position. After placing Mg^{2+} ions and water molecules in the difference density peaks, further rounds of refinement provided us with a reasonable 2mF_o-F_c density map in the active site of both monomers (Fig. EV3A,B, *right panel*) and the POLDER (Omit) maps indicate a good fit of the compound to the density (Fig. EV3A,B*, bottom left panel*). Finally, the TmPPase:ETD structure was refined to an average resolution of 3.2 Å (h = 3.1 Å, k = 3.6 Å, l = 4.3 Å) with the final R_{work}/R_{free} of 27.2% / 31.0 % (Table S1).

Similarly, the initial refinement of TmPPase:ZLD revealed positive (F_o-F_c) density at 3σ that could accommodate ZLD in all four chains in the asymmetric unit (Figs. EV4A-D, *upper left panel*). After placing Mg^{2+} ions and water molecules in the difference density peaks, further rounds of refinement provided us with a 2mF_o-F_c density map in the active site for all monomers (Fig. EV4A-D, *right panel*) and was validated by POLDER (Omit) maps (Figs. EV4A-D*, bottom left panel*). The final refinement shows that the TmPPase:ZLD structure has an average resolution of 3.3 Å (h = 4.5 Å, k = 4.2 Å, l = 3.2 Å) with a final R_{work}/R_{free} of 25.9 % / 30.4 % (Table S1).

Asymmetry in the TmPPase complex with etidronate

Unlike the fully-open TmPPase:Ca:Mg structure (PDB ID: 4AV3), we observed additional density above the hydrolytic centre in both chains that could be fitted with several residues of loop5-6 (Fig. 2A and Fig. EV5). This left eight residues (V208$^{5.67}$-L215$^{5.74}$) in loop5-6 of chain A and three residues (L213$^{5.72}$-L215$^{5.74}$) in chain B unmodeled due to the lack of extra density. In the IDP-bound structure[45], these loops interact with IDP and form a tightly packed structured lid over the active site. However, in the TmPPase:ETD structure, despite interacting with ETD in both chains, these loops are positioned slightly above the active site (Fig. 2B-D), with loop5-6 of chain A extending more toward the centre compared to loop5-6 of chain B (Fig. 2A).

Structural alignment between chain A and B of TmPPase:ETD yields a root mean square deviation (RMSD) per Cα of 1.44 Å, approximately four times higher than the RMSD between chain A and B in the resting state (RMSD/Cα= 0.39 Å) (Table S2). Despite the overall structural similarity, further comparison between the monomers of TmPPase:ETD and those in the resting state reveals that chain

B of TmPPase:ETD differs most from TmPPase:ETD chain A and from both chains in the resting state structure (Table S2). Notably, there are clear differences on the cytoplasmic (hydrolytic) side between the monomers of TmPPase:ETD; chain B adopts a slightly more constricted conformation compared to chain A (Fig. 2A). Bendix analysis[46] showed that three (TMH11, 12 and 15) out of six inner ring helices of chain B are more curved on the cytoplasmic side, bending towards the active site (Fig. EV6). Besides that, the loops on the cytoplasmic side of chain B (loops11-12, 13-14, and 15-16) appear to be more flexible, as indicated by more unresolved residues, compared to those in chain A (Fig. 2A). These observations suggest structural asymmetry between chains A and B in the TmPPase:ETD structure.

The structural asymmetry arises due to differences in the orientation of ETD within each monomer at the active site. ETD comprises two phosphonate groups separated by a central carbon bonded to a hydroxyl group. Compared to the IDP location in the IDP-bound structure, ETDs are positioned above the IDP site, with the lower phosphonate group of ETDs located in the position of the upper (leaving-group) phosphonate group of IDP (Fig. 2B). However, the upper phosphonate group of ETDs in chains A (ETD_A) and B (ETD_B) is distinctly positioned; ETD_A is tilted approximately by 35.9° relative to the IDP orientation, while ETD_B is relatively parallel to the IDP orientation (Fig. 2B). The lower phosphonate group position remains the same for both ETDs (Fig. 2B). As a result, loop5-6 of the two monomers is oriented differently. In chain A, this loop protrudes towards the active centre and interacts with ETD_A *via* E217$^{5.76}$ mediated by a Mg^{2+} ion, while in chain B, the loop is more constricted and interacts with ETD_B *via* D218$^{5.77}$, also mediated by a Mg^{2+} ion (Fig. 2B,C and D). Furthermore, ETD_A and ETD_B interact with the active site *via* different residues (Fig. 2C,D). D465$^{11.57}$, D488$^{12.39}$ and N492$^{12.43}$ in TMH11 and TMH12 were involved in the interaction with ETD_B *via* a water molecule. Consequently, these two TMHs undergo slight inward movement, resulting in a more constricted conformation of chain B. Nonetheless, the methyl group of ETDs in both chains points towards TMH12 (Fig. 2C,D), which might prevent complete closure of the hydrolytic centre and downward motion of TMH12.

Structural distinction between zoledronate and IDP-bound TmPPase

In contrast to the TmPPase:ETD structure, the TmPPase:ZLD structure adopts a closed conformation, The overall structure is more similar to the IDP-bound structure (RMSD/Cα of 0.760 Å) than the resting state structure (RMSD/Cα of 2.32 Å) (Table. S2). However, compared to the IDP-bound structure, the TmPPase:ZLD structure exhibits noticeable movements in three of six inner ring helices (TMH11, 12 and 15) and seven of ten outer ring helices (TMH1-4 and 7-9). These movements extend outwards from the hydrolytic centre (Fig. 3A), leaving it not fully closed. A cross-sectional view confirms this observation, showing the tunnel extending from the hydrolytic centre to the enzyme opening, which

is closed in the IDP-bound structure (Fig. 3B,C). This is because ZLD is bulkier than IDP due to the presence of the heteroaryl group, which points towards TMH11, 12, and 15 on the cytoplasmic side.

Although the hydrolytic centre of TmPPase:ZLD is more open, the coordination of the Mg_4ZLD complex with the active site residues closely resembles that of Mg_5IDP in the IDP-bound structure (Fig. 3E,F). ZLD is nonetheless positioned about 1.0 Å above IDP (Fig. 3D) because it is bulkier. However, unlike the IDP-bound structure, and, even though the arrangement of TMHs in the ion gate is almost identical, we did not observe any density for a Na^+ in the TmPPase:ZLD structure despite its higher resolution (*i.e.* 3.26 Å compared to 3.5 Å for the IDP-bound structure) (Fig. EV7C).

Exit channel and active site lid movements

The X-ray structures of TmPPase with the different inhibitors bound to the active site show either a closed, resting or asymmetric (TmPPase:ETD, Fig. 2) conformation. The asymmetric structure of the TmPPase with ETD is unique and similar to that observed in our recent time-resolved study[7]. To probe the TmPPase conformational ensemble in solution under various inhibitor-bound conditions, we employed DEER spectroscopy. We selected two distinctive sites on TmPPase (S525 and T211), which were mutated to cysteine and selectively spin-labelled with 2,5-dihydro-2,2,5,5-tetramethyl-3-[[(methylsulfonyl)thio]methyl]-1*H*-pyrrol-1-yloxy (MTSSL, modification is denoted as R1 hereafter) to enable the measurement of interspin distances between the spin-labelled residue pairs. The selected sites were located on the exit channel (S525R1) and the enzyme entrance (T211R1) to capture any conformational changes occurring in the protein on either side of the membrane (Fig. 4A and Fig. EV8A) without interfering with the activity of TmPPase. For both TmPPase sites, high mPPase spin labelling efficiency was achieved with no non-specific MTSSL being present, as evidenced by the continuous wave electron paramagnetic resonance (CW EPR) spectra recorded at room temperature (Fig. EV9) [47-49]. From the CW EPR spectral lineshapes (Fig. EV9), which relate to the rotation correlation time of the spin label, we observed that T211R1 showed high spin label mobility in the conditions tested (apo, +ETD, and +IDP), while S525R1 had intermediate to low spin label mobility in the conditions tested (apo, +Ca, +Ca/ETD and +ETD). This is consistent with spin-labelled sites on integral membrane proteins of variable dynamics[30-32]. Unlike DEER, which provides insights into the conformational state of membrane proteins[30], CW EPR offers information on the local environment of the spin label. The results show no significant difference in the local environment at either site between the *apo* state and the inhibitor-bound state.

In addition, we generated *in silico* distance distribution predictions for the two sites (S525R1 and T211R1) using MtsslWizard[50] and based on the X-ray structures of TmPPase with different molecules

bound (Fig. 4, Fig. EV8). In the case of T211R1, the X-ray electron density in $loop_A$5-6 of the TmPPase:ETD (residues V208$^{5.67}$-L215$^{5.74}$: VGKTELNL) and TmPPase:Ca (residues T211$^{5.70}$-R221$^{6.28}$: TELNLPEDDPR) structures is missing, suggesting a highly dynamic or disordered state for this region. We therefore modelled this protein region using the Rosetta server[51] and generated *in silico* distance distributions based on the X-ray structures. These were overlaid with the experimentally derived DEER distance distributions (Fig. 4D, Fig. EV8D) for comparison. The S525R1 dimer yielded high-quality DEER traces, allowing us to resolve the distance differences between the inhibitor conditions probed. Under all tested conditions, strong oscillations were observed in the raw DEER data (Fig. 4B) indicating that the shifts observed in the state populations within the TmPPase ensemble are highly reliable. Both DeerAnalysis and ComparativeDeerAnalyser were used for background correction of the DEER traces and their results are in agreement (Fig. 4C and Fig. EV8B).

The separation of S525R1 in the *apo* state (with no Ca^{2+} or inhibitor added) is broad with a mean distance of 3.8 nm (Fig. 4D). In the presence of Ca^{2+}, the distance distribution shifts towards shorter distances, suggesting that the two monomers come closer at the periplasmic side, and consistent with the predicted distances derived from the TmPPase:Ca structure. In the presence of both Ca^{2+} and ETD (+Ca/ETD), we observe an increase in the mean distance distribution to 3.7 nm, consistent with the predicted distance for the TmPPase:ETD structure (which corresponds to the +Ca/ETD condition). Finally, in the presence of ETD but no Ca^{2+}, the experimental distance between the loops on the different monomers increases to 4.0 nm. Although these changes are small, they are significant. They can be seen in both the time domain data (Fig. 4C) and resulting distances (Fig. 4D) . The reference black dashed lines depicted for the *apo* state, highlight these subtle changes in the background corrected time traces. More substantial changes occur with the addition of IDP with a mean of the resulting distance distribution at 4.2 nm, which is the longest distance recorded for the S525R1 pair in solution. In contrast, the addition of ZLD results in the shortest distances we observed by DEER under the conditions tested, with a mean of the distance distribution of 3.4 nm. Remarkably, this differs substantially from the *in silico* distance distribution predicted from the X-ray structure of TmPPase:ZLD (4.3 nm), which is expected to be identical to that of TmPPase:IDP (RMSD/Cα = 0.571 Å) (see Discussion).

Unlike S525R1, distance distributions for T211R1 derived from the DEER time traces are broad for all conditions tested (Fig. EV8D). This is evidenced by the lack of oscillations in the raw DEER data (Fig. EV8B), which further supports the highly dynamic nature of the labelling site located on $loop_A$5-6. The lack of electron density in the respective X-ray structures is due to flexibility, also consistent with the high mobility recorded in our CW EPR spectra at room temperature (Fig. EV9A). DeerAnalysis and ComparativeDeerAnalyzer are in close agreement, as in the case of S525R1 (Fig. EV10). For *apo* and

+Ca/ETD in particular, traces were collected for longer time windows to resolve longer distances for the T211R1 pair (Fig. EV8B). The broad distance distributions suggest the conformational flexibility of T211R1 (Fig. EV8C). The *apo*, +Ca and +Ca/ETD conditions all appear highly similar, while the obtained distributions for +ETD and +IDP have larger contributions from shorter distances within their conformational ensembles. Finally, TmPPase incubated with ZLD (TmPPase+ZLD) in solution appears to have longer distances, contrasting with predictions derived from the TmPPase:ZLD structure.

Collectively, periplasmic S525R1 allows for robust quantitative interpretations of the conformational transitions TmPPase undergoes under different conditions. T211R1 presents a highly dynamic site with less defined oscillations in the DEER traces. However, the overall transitions suggested by T211R1 agree qualitatively with conformational changes informed by the S525R1 pair: upon substrate/inhibitor binding, the T211R1 pair moves closer while the S525R1 pair distance increases.

Based on the DEER data on the IDP-bound TmPPase, we observed significant deviations between the experimental and the *in silico* distances derived from the TmPPase:IDP X-ray structure for both cytoplasmic- (T211R1) and periplasmic-end (S525R1) sites (Fig. 4D and Fig. EV8D). This deviation could be explained by the dimer adopting an asymmetric conformation under the physiological conditions used for DEER, with one monomer in a closed state and the other in an open state. To model this asymmetric arrangement, we combined chain A of the TmPPase:Ca structure with chain B of the TmPPase:IDP structure, *i.e.* TmPPase:Ca(A)_IDP(B), and predicted its *in silico* distance distribution (Fig. 5A). Remarkably, the derived asymmetric model predicts a distance distribution that agrees closely with the experimental DEER distance distribution obtained for S525R in solution (Fig. 5B). This predicted distribution also falls between the two conformational extremes of TmPPase (Fig. 4D and 5B).

Effect of ETD and ZLD on sodium transport of TmPPase

Previously, we showed that IDP can facilitate a single Na^+ pumping cycle without hydrolysis[7]. To investigate whether pumping also occurs in the presence of ETD and ZLD, we recorded electrometric data during PP_i hydrolysis and after binding of IDP, ETD and ZLD. In electrometric measurements, also known as solid-supported membrane-based electrophysiology[52], a current signal is generated and recorded when Na^+ is transported across the membrane by the active reconstituted TmPPase. A maximal positive signal of 0.6 $\pm$ 0.025 nA was detected within 0.15 ns (excluding instrument dead time) after the addition of 100 µM substrate K_4PP_i (Fig. 6A). Most of the signal decayed within 1 second after K_4PP_i was supplied. Full signal recovery required several minutes before a repeat measurement could be performed on the same sensor. As expected, when 200 µM K_2HPO_4 was added as a negative

control, there was no signal, indicating that no ion pumping had occurred. Replacing the substrate with IDP resulted in a signal about half that of K_4PP_i. However, in the presence of 50 µM ETD or 50 µM ZLD, the signals were barely detectable, indicating no Na^+ pumping was observed.

This observation is consistent with the TmPPase:ETD and TmPPase:ZLD structures, which show the absence of Na^+ density in the ion gate. Interestingly, in all the solved TmPPase structures, Na^+ at the ion gate has only been observed in the IDP-bound structures (Fig. 6B-E and Fig. EV7). In the IDP-bound structure, four key residues ($D703^{16.46}$, $D243^{6.50}$, $S247^{6.54}$ and $E246^{6.53}$) in the ion gate constitute the Na^+ binding site (Fig. 6E). The formation of the site is driven by the downward motion of TMH16 (Fig. EV7A), transitioning from the resting state (TmPPase:Ca) to the closed state (TmPPase:IDP). The orientation of $D703^{16.46}$ of the TmPPase:ETD structure resembles the structure of TmPPase:Ca, rotated away from the Na^+ binding site, causing a loss of Na^+ binding (Fig. 6B,C). In the TmPPase:ZLD structure, $D703^{16.46}$ and $K707^{16.50}$ are oriented relatively similarly to the Na^+ binding position in the TmPPase:IDP structure (Figs. 6D,E and Fig. EV7C), but no Na^+ density was observed despite the higher resolution compared to the TmPPase:IDP structure (3.26 Å compared to 3.5 Å for the IDP-bound structure). This might be because the inhibitor restricts the complete closure of the active site and full constriction and downward movement of the inner helices (especially TMH12 and 16) (Fig. 3A-D), which hinder the Na^+ pumping.

Discussion

Inhibition of TmPPase by bisphosphonates

The seven distinct bisphosphonates we tested exhibit varying levels of inhibition against TmPPase (Fig. 1B). ETD and IBD exhibited higher IC_{50} values compared to PMD, ALD, and NRD (p <0.0001) (Fig. 1B). This is consistent with the K_i of ETD on DhPPase (mPPase of *Desulfitobacterium hafniense*), which is approximately 67 times higher than that of amino methylene diphosphonate (AMDP), as measured by Viktor *et al.*,[22,53]. The difference may be due to the introduction of an amino group in the side chain and the length of the side chain[41]. Substituting the hydrogen (in ETD) with the benzene ring (in ZLD and RSD) does not favour inhibitory activity (IC_{50} > 200 µM). Nonetheless, these aromatic-containing compounds are still capable of preventing NEM modification on TmPPase (Fig. 1C), as furhter supported by the solved structure of ZLD bound with TmPPase (see discussion below).

Catalytic asymmetry in mPPase

Some evidence for asymmetry in mPPase gating has been shown previously by kinetic studies[7,22] and captured in the time-resolved 600s and 3600s structures of TmPPase:PP_i[7], where in both structures, one chain is in the open state and the other is in the closed state. Our new structures, together with DEER distance measurements that monitor the conformational ensemble equilibrium of TmPPase in solution, provide further solid experimental evidence of asymmetry in gating and transitional changes upon substrate/inhibitor binding.

In our study, the TmPPase:ETD structure captured the asymmetric binding of ETD (Fig. 2). Loop5-6, which interact with ETD, moves inward to close the active site, but not as deeply as in the TmPPase:IDP structure (Fig. 2A,B). Here, ETD is positioned[22] above the hydrolytic centre (Fig. 2B), unable to descend further due to occupation of the Ca^{2+} in the active site (Fig. 2C,D), as in the TmPPase:Ca structure (PDB ID: 4AV3). This is supported by our DEER data recorded in solution, which showed an enhancement of the longer distance distribution components of T211R1 when comparing the +ETD-only to the +Ca/ETD condition (Fig. EV8D), indicating a semi-closed conformation. While in the absence of Ca^{2+}, the loops move closer together. Due to the different orientations of ETD in the two monomers, the orientations of loop5-6 differ as well (Fig. 2A,B). Nevertheless, the TmPPase:ETD structure can be considered as a snapshot transition between the *apo* structure (TmPPase:0-60s, PDB: 8B21), where no substrate is bound, and the TmPPase:600s structure (PDB: 8B23), where the PP_i has bound to one chain and descended to the hydrolytic centre. On the other hand, the TmPPase:ZLD structure, while

resembling the IDP-bound structure, is more open (Fig. 4) and ZLD is positioned about 1.0 Å above the IDP position in the hydrolytic centre (Fig. 3D)[7].

Based on these observations, and the DEER data for +IDP, which is consistent with an asymmetric conformation of TmPPase being present in solution, we propose five distinct models of TmPPase (Fig. 7). All these models involve one monomer in an open/resting state, while the other is constrained upon the binding of the substrate/inhibitors. Model 1 (Fig. 7), where both monomers are in the resting state as in the TmPPase:Ca structure[8], displays both active sites in an open conformation. In model 2 (Fig. 7), one active site is semi-closed, while the other remains open. This is supported by the distance distributions for S525R1 and T211R1 for +Ca/ETD informed by DEER, which agrees with the *in silico* distance predictions generated by the asymmetric TmPPase:ETD X-ray structure.

While models 1 and 2 differ at the active site, the DEER distance distributions recorded for the S525R1 pair in the near exit channel are highly similar (Fig. 7, models 1 and 2). However, in the presence of ZLD, and as seen in model 3 (Fig. 7), the mean of the DEER distance distribution for S525R1 is shifted towards shorter distances (3.4 nm), while the active site (T211R1) retains the configuration observed in model 2. This might be because, although ZLD can enter the active site, its bulky heteroaryl group prevents the complete closure of the active site and restricts the full downward movement of TMH12 and TMH16. This likely prevents the formation of the Na^+-binding site, leading to the absence of Na^+ in the TmPPase:ZLD structure (Fig. 3) and the lack of Na^+ signal in the electrometric measurement (Fig. 5).

Among all conditions tested, the DEER distance distributions of IDP-bound TmPPase exhibit the longest distances recorded for the periplasmic S525R1 site, but the shortest for the cytoplasmic T211R1 site. This suggests that the binding of IDP to TmPPase induces the closure of the active site and the full downward movement of TMH12 and TMH16, in line with the IDP-bound TmPPase structure. However, the DEER distance distributions obtained in solution for both S525R1 and T211R1 fall in between the extreme modelled distances seen in the X-ray structures. This is due to the presence of an asymmetric conformation between the two monomers, consistent with the asymmetric binding model (Fig. 7, model 4,5), where IDP (and similarly for ETD without Ca^{2+} present) binds only to one monomer, as in the hybrid structure TmPPase:Ca(A)_IDP(B) (Fig. 5A).

These models further confirm structural and functional studies showing the asymmetry in the catalysis of TmPPase. Together with our previous time-resolved structures[7], they complement the ensemble of conformational changes during the reaction steps.

Sodium ion pumping in TmPPase

In a previous study[7], we found that the single turnover event of Na^+ pumping only occurs in the presence of IDP. In our current Nanion SURFE^{2}R experiment, upon the addition of ETD and ZLD, we did not observe Na^+ pumping (Fig. 5A), consistent with ETD and ZLD bound structures where no Na^+ was observed at the ion gate.

We proposed that the motion of TMH12 and the communication network from TMH5 to TMH13 and TMH10 are key parts of intra-subunit communication between the two monomers[7,20]. Loop12-13, where the S525R1 site is located, can be used to monitor the motion of TMH12. The mean distance for the S525R1 distribution in the *apo* state is shorter compared with the IDP bound state (Fig. 4D). However, in the presence of ZLD, the distances for S525R1 are even shorter than in *apo*, contradicting our initial prediction of having similar distances to the IDP bound state. This suggests that in solution, the exit channel of the ZLD-bound TmPPase can adopt a conformation that resembles the *apo* state, even though its active site is similar to the IDP-bound condition. This may explain why TmPPase is unable to pump Na^+ upon the addition of ZLD. We suggest that while IDP constrain the conformation of one subunit to a closed state as in model 4 (Fig. 4D) and facilitate single turnover events of Na^+ transport[45], ZLD and ETD restrict the conformation of one subunit to an intermediate state as in models 3 and 5 (Fig. 7), which is unable to facilitate Na^+ transport.

In summary, EPR experiments in solution, coupled with new structures of inhibited forms of TmPPase, reveal that TmPPase binds inhibitors asymmetrically, forming open-closed states, where one monomer is in the inhibitor (IDP, ETD, ZLD) bound state and the other monomer is in the open state, consistent with half-of-the-sites-reactivity[7]. In future studies, we could use time-resolved DEER in complex with the substrate to explore, for example, how and in what order the release of phosphate products and ions leads to conformational changes in the active sites, exit channels, and communication between subunits, capturing further details during the reaction steps.

Materials and Methods

Protein expression and purification

TmPPase expression and purification have been described previously [54,55]. Briefly, pRS1024 plasmid containing his-tagged TmPPase was freshly transformed into *Saccharomyces cerevisiae* strain BJ1991. The cells were cultured in 250 ml of selective synthetic complete drop-out (SCD) media overnight before being added to 740 ml of 1.5× YP media with 2% glucose. The cells were then cultured for 8 h at 30 °C, collected by centrifugation (4,000 rpm, 10 min) and lysed at 4 °C using a bead beater with 0.2 mm glass beads. The membrane fraction was collected by ultracentrifugation (100,000 × g, 45 min) and the pellets were resuspended in buffer containing 50 mM MES-NaOH pH 6.5, 20% (v/v) glycerol, 50 mM KCl, 5.2 mM $MgCl_2$, 1.33 mM dithiothreitol (DTT), 2 µg ml-1 (w/v) pepstatin-A (Sigma) and 0.334 mM PMSF (Sigma). The membranes were solubilised in solubilisation buffer (50 mM MES-NaOH pH 6.5, 20 % (v/v) glycerol, 5.33 % (w/v) n-dodecyl-β-D-maltopyranoside (DDM) (Anatrace)) using the 'hot-solve' method [55] at 75 °C for 1.5 h. After centrifugation to remove denatured proteins, KCl (to a final concentration of 0.3 M) and 2 ml of Ni-NTA beads (Qiagen) were added and incubated at 40 °C for 1.5 h, and then loaded into an Econo-Pac® column (Bio-Rad). Then the column was washed with two column volume (CV) of washing buffer (50 mM MES-NaOH pH 6.5, 20% (v/v) glycerol, 50 mM KCl, 20 mM imidazole pH 6.5, 5 mM $MgCl_2$, 1 mM DTT, 2 mg/ml (w/v) pepstatin-A, 0.2 mM PMSF and 0.05% DDM (Anatrace) and eluted with 2 CV of elution buffer (50 mM MES-NaOH pH 6.5, 3.5% (v/v) glycerol, 50 mM KCl, 400 mM imidazole pH 6.5, 5 mM $MgCl_2$, 1 mM DTT, 2 mg/ml (w/v) pepstatin-A, 0.2 mM PMSF and 0.5% octyl glucose neopentyl glycol (OGNPG, Anatrace).

TmPPase activity assay

TmPPase activity and bisphosphonates inhibition assay were performed using the molybdenum blue reaction method in 96-well plate format as reported previously[42]. Before the assay, the enzyme was reactivated by adding to the mixture of 30 mg/ml of soy-bean lecithin (Sigma) in 20 mM Tris-HCl pH 8.0 with 4.5% DDM and incubated at 55 °C for 15 min. The activity reaction was done in the reaction buffer (60 mM Tris-HCl pH 8.0, 5 mM $MgCl_2$, 100 mM KCl, and 10 mM NaCl) and started by adding 2 mM Na_4PP_i at 71°C for 5 min.

NEM modification assay

The NEM modification assay was performed as reported previously[8,56] with slight modification. Briefly, 0.4 mg/ml of the reactivated TmPPase was mixed with the modification buffer (20 mM MES-KOH pH

6.5, 0.05% DDM, 2.4 mM $MgCl_2$, 100 mM KCl, and 20 mM NaCl) and different inhibitors (2 mM $CaCl_2$, 0.5 mM IDP, and 0.5 mM of bisphosphonates) and incubated on ice for 30 min. Afterwards, 100 mM *N*-ethyl maleimide (NEM) (Thermo Scientific) was added and the mixture was further incubated for 10 min. The NEM-modification reactions were stopped by adding 2 mM DTT and the residual activity of the enzyme was performed using the molybdenum blue reaction assay[57].

Crystallisation and structure determination

For co-crystallisation with bisphosphonates, the purified TmPPase was buffer exchanged to the crystallisation buffer (50 mM MES-NaOH pH 6.5, 3.5% (v/v) glycerol, 50 mM KCl, 5 mM $MgCl_2$, 2 mM DTT and 0.5% OGNPG) on a Micro Bio-Spin 6 column (Bio-Rad) and then diluted to a concentration of 10 mg/ml. Prior to crystallisation, 1 mM bisphosphonates was added to the protein solution, incubated at room temperature for 30 min, and centrifuged for 20 min (16,000 g, 4 °C). Crystallisation trials were done using a Mosquito robot (SPT Labtech) by sitting drop vapour-diffusion method using MemGold™ screen (Molecular Dimensions) in MRC 2-well crystallisation plates (Swissci), and the drops were monitored at 22 °C using the minstrel DT UV imaging system (Formulatrix). Crystal hits appeared on the MemGold™ screen under different conditions. Harvestable crystals appeared within several days and were frozen directly from the mother liquor. For the TmPPase cocystallised with etidronate, the best diffracting crystal was observed from a solution containing 0.2 M $CaCl_2$, 0.1 M HEPES pH 7.0, and 33% PEG400, while for TmPPase cocrystallised with zoledronate, the best diffracting crystal was observed from a solution containing 0.1 M MES pH 6.5, 0.1 M NaCl, 33% PEG400, and 4% ethylene glycol.

X-ray diffraction data were collected at Diamond Light Source (DLS) (UK) on the I03 (TmPPase:ETD) and I04-1 beamline (TmPPase:ZLD) at 100 K on a Pilatus 6M detector. The data were merged and scaled using X-ray Detector Software (XDS)[58] and the structure was solved by molecular replacement with Phaser [59] using the resting state (4AV3)[8,56] and IDP-bound (5LZQ) state[9] of TmPPase structure as the search model for TmPPase:Etidronate and TmPPase:Zoledronate, respectively. The structures were built and refined using phenix.refine [60] and Coot [61]. X-ray data and refinement statistics are listed in Table 1.

EPR Spectroscopy

Sample preparation for EPR spectroscopy

For EPR spectroscopy measurements, residue S525, located in the periplasmic loop12-13 of the TmPPase exit channel, was mutated to cysteine and covalently modified with a methanethiosulfonate thiol-specific spin label (MTSSL) to introduce a paramagnetic centre[62,63] (the labelled protein is referred to as S525R1). At the cytoplasmic side of the membrane interface, we constructed the TmPPase T211C variant, which is located in loop5-6 and above the active site (the MTSSL labelled mutant is referred to as T211R1).

The S525C and T211C proteins were expressed as outlined above. The frozen cell pellets were lysed using cryo-milling (Retsch model MM400). 1 mM TCEP was used to replace DTT in the purification steps preceding spin labelling and the remaining purification was carried out as above. Each protein was spin-labelled with MTSSL while immobilised to the Ni-NTA resin (or mixed following Cys mutant elution) as previously described[39,48]. Briefly, for MTSSL labelling, MTSSL was added in spin-label buffer (20 mM MOPS-NaOH, 1 mM TCEP, 5 mM $MgCl_2$, 50 mM KCl, 3.5% glycerol, 0.03% DDM at pH 7.5) at 10-fold molar protein excess and incubated for 2 hours at room temperature. Spin-labelled protein was eluted from the Ni-NTA resin column, concentrated and subsequently purified using size-exclusion chromatography using Superose 6 increase 10/300 GL (GE Healthcare) and equilibrated in 20 mM MES-NaOH, pH 6.5, 5 mM $MgCl_2$, 50 mM KCl, 3.5% glycerol, 0.05% DDM. The eluted purified protein fractions were concentrated, buffer exchanged with buffer prepared in D_2O, and split into aliquots for incubation with a final concentration of 2 mM of inhibitors or 10 mM $CaCl_2$ (30 min, RT). The protein activity was tested as described above, and the protein samples were tested for spin labelling by CW EPR spectroscopy, and then 40 % ethylene glycol-d_6 was added to each sample before flash freezing for DEER measurement.

Continuous Wave EPR (CW EPR) spectroscopy

CW EPR experiments were performed on a Bruker Magnettech ESR5000 X-band spectrometer. The spin-labelled sample was loaded into an EPR tube before the addition of ethylene glycol-d_6. The samples were measured at room temperature, as TmPPase is more thermally stable than most membrane proteins. The measurements were performed in a 330-345 mT magnetic field, with a 60 s sweep time, 0.1 mT modulation, 100 kHz frequency, and 10 mW (10 dB) microwave power.

Double Electron-Electron Resonance (DEER, or PELDOR) spectroscopy

DEER distance measurements and set-up

EPR recordings were collected as previously described[64] using a Bruker ELEXSYS E580 Spectrometer operating at Q-band frequency, equipped with a QT-II resonator in a Cryogenic Ltd. cryogen-free variable temperature cryostat for EPR. In brief, spin-labelled protein samples were prepared in 3 mm outer diameter quartz tubes and data was recorded at 50 K. The detection pulse sequence used was a refocused Hahn echo: $\pi/2$ - $\tau1$ - π - $\tau1$ - $\tau2$ - π - $\tau2$ - echo, with $\pi/2$ and π pulse lengths of 32 ns, $\tau1$ of 380 ns and $\tau2$ of 2000 ns. In all cases, the frequency of the detection pulses was 33.96 GHz, and a 16 ns pump pulse of 34.025 GHz was moved in 4 ns increments in the gap between the two π pulses of the detection sequence to yield the DEER trace. All pulses were generated using an integrated Bruker SpinJet AWG, and a 16-step phase cycle on the detection pulses was used to remove unwanted echo crossings [65]. Traces were recorded at a magnetic field of 12111 G, setting the pump pulse resonant with the nitroxide spectral maximum. Scans were recorded until a sufficient signal-to-noise ratio was obtained, typically with datasets averaged overnight.

DEER data analysis and processing

Distance distributions were determined from the time traces using various methodologies as this becomes a good practice to get reliable results and to show consistency between different approaches. In the present work, we used two different programs, DeerAnalysis[66,67] and ComparativeDeerAnalyzer[67] which are MATLAB-based programs. Data were processed using DeerAnalysis2022. The data were loaded, the “2+1” artefact truncated from the dataset (-600 ns)[68], then phase and background corrected using the ‘!’ automated adjustment. The background corrected traces were then transformed from the time domain to the distance domain using Tikhonov Regularization[69], and the quality of the fit was assessed based on the L-curve method and the shape of the Pake pattern. The resultant background correction was then validated using a module for validation implemented in DA. The validation was carried out after initial Tikhonov regularisation, varying the background start time from 5% to 80% of the respective time windows of the cut data for 16 trials. From this, the raw data were re-loaded and processed (Tikhonov regularisation) with the cutoff and background start time as established from the first round of validation. Resulting data are taken for plotting figures showing raw data/background and form factor/fit. This is the starting point for a full validation, where the background start time was again varied from 5% to 80% of the time window for 16 trials, as well as some added "white noise" with a level of 1.50 for 50 trials. The result of validation was pruned and used for plotting the distance distribution and confidence interval. We have also used the ComparativeDeerAnalyser (CDA) feature implemented in DeerAnalysis 2022 which is an automated process that uses three approaches simultaneously to assess and reduce model bias by comparing their associated results.

In silico spin labelling and modelling

MttslWizard[50] was used to analyse the labelling sites of TmPPase to predict the shifts in distance distribution under different conditions. The PDB coordinates of the respective X-ray structures (TmPPase:Ca, TmPPase:Ca:ETD, TmPPase:ZLD, and TmPPase:IDP) for the different conditions were uploaded to the online MTSSL Suite server, labelled at T211 and S525 sites (both monomer A and B) using the mode 'tight 0 clashes allowed'. The distance distributions were then calculated. The distance distribution data were exported to Prism 10 (GraphPad) to plot the distance distribution graphs.

Electrometric measurement

For the Nanion SURFE^{2}R experiment, purified TmPPase was reconstituted into liposomes as previously described[45] with some modifications. Briefly, the purified protein was buffer exchanged into a reconstitution buffer (50 mM MOPS-KOH pH 7.2, 50mM KCl, 5mM $MgCl_2$, and 2mM DTT) to remove Na^+ and glycerol and then diluted to 50 μg/ml concentration. 15 μl of liposome solution (120 mg/ml soy-bean lecithin in 50 mM MOPs-KOH pH 7.2) was mixed with 1 ml of diluted protein sample. SM-2 Bio-beads were added in increments to a final concentration of 0.25 mg/μl and then placed into a mixer at 4 °C for 6 h to ensure beads stayed in suspension. The proteoliposomes were collected and frozen at -80 °C in aliquots. To ensure that the reconstituted protein was still active, the hydrolytic activity was performed using the molybdenum blue reaction assay[57].

Electrometric measurements were performed on a SURFE^{2}R N1 instrument from Nanion Technology (Munich, Germany). The gold sensors were prepared based on the 'SURFE^{2}R N1 protocol', including thiolation of the sensor surface and assembly of the lipid layer using sensor prep A2 and B solutions. 15 μl of sonicated proteoliposomes, followed by 50 μl of the rinsing buffer (50 mM MOPS-KOH pH 7.2, 50 mM NaCl, 5 mM $MgCl_2$) were applied directly to the sensor surface. Sensors were centrifuged for 30 minutes at 2500 g and incubated at 4 °C for 3 h. The sensors were mounted in the SURFE2R N1 and rinsed once with 1 ml of rinsing buffer (50 mM MOPS-KOH, pH 7.2, 50 mM NaCl, 5 mM $MgCl_2$). Measurements were performed for 3 s by consecutively flowing non-activating buffer B (50 mM MOPS-KOH pH 7.2, 50 mM NaCl, 5 mM $MgCl_2$, 200 μM K_2HPO_4) and activating buffer A (50 mM MOPS-KOH, 50 mM NaCl, 5 mM $MgCl_2$) containing substrate (100 μM K_4PP_i) or inhibitors (50 μM IDP, 50 μM ETD or 50 μM ZLD) across the sensor for 1 s each in a BAB sequence. Charge transport across the membrane is initiated by substrate or inhibitor in buffer A, which flows across the sensor between 1

and 2 s. The transport of positively charged ions during this period results in a positive electrical current, the signal output of the SURFE2R N1 instrument. Between each measurement, the sensor was washed with 1 ml rinsing buffer and incubated for 60 seconds. The measurements were tested in triplicates.

Acknowledgements

This work was supported by the Biotechnology and Biological Research Council (BBSRC) (BB/T006048/1) awarded to C.P. and A.G. Grants from the Academy of Finland (No. 1322609 & 13364501) to A.G., (No. 308105 and 1355187) to K.V., and (No. 310297) to H.X., also supported part of this work. The first author is funded by the China Scholarship Council (CSC) from the Ministry of Education of P.R. China. The authors thank Juho Kellosalo for fruitful discussions during the project. EPR measurements were performed at the national EPR facilities in Manchester and the BioEmPiRe Centre for Structural Biological EPR spectroscopy funded by BBSRC (BB/W019795/1) to C.P. We thank Diamond Light Source for access to beamline I03 and I04-1. The facilities and expertise of the HiLIFE Crystallization unit at the University of Helsinki, a member of FINStruct and Biocenter Finland are gratefully acknowledged.

Author contributions

Conceptualisation, JL, KV, CP, HX, AG; Methodology, JL, KV, AS, KH, ABr, ABo, AG, CP, NGJ, LJ, Investigation, KV, JL, AS, YM, OR; Resources, AG, CP, KV, NGJ, HX, JYK.; Writing – Original draft, JL, AS, KV, CP; Writing-Review and Editing, JL, KV, NGJ, CP, AS, LJ, JYK, HX, AG; Visualization, KV, CP, AS, JL; Supervision and Project Administration, AG, CP, HX, JYK.; Funding Acquisition, JL, KV, CP, AG, HX, JYK.

Declaration of interests

All authors declare no conflict of interest in this paper.

Data availability

The atomic coordinates and structure factors of the TmPPase:Etidronate and TmPPase:Zoledronate complex have been deposited in the Protein Data Bank, www.rcsb.org (PDB ID: 9G8K and 9G8J).

References

1 Baltscheffsky, H., von Stedingk, L.-V., Heldt, H.-W. & Klingenberg, M. Inorganic pyrophosphate: formation in bacterial photophosphorylation. *Science* **153**, 1120-1122 (1966). https://doi.org/10.1126/science.153.3740.1120

2 Karlsson, J. Membrane-bound potassium and magnesium ion-stimulated inorganic pyrophosphatase from roots and cotyledons of sugar beet (*Beta vulgaris L.*). *Biochim. Biophys. Acta* **399**, 356-363 (1975). https://doi.org/10.1016/0304-4165(75)90264-0

3 Rea, P. A. *et al.* Vacuolar H^+ -translocating pyrophosphatases: a new category of ion translocase. *Trends Biochem. Sci.* **17**, 348-353 (1992). https://doi.org/10.1016/0968-0004(92)90313-x

4 Baykov, A. A., Malinen, A. M., Luoto, H. H. & Lahti, R. Pyrophosphate-Fueled Na+ and H+ Transport in Prokaryotes. *Microbiol. Mol. Biol. Rev.* **77**, 267-276 (2013). https://doi.org/10.1128/MMBR.00003-13

5 Serrano, A., Perez-Castineira, J. R., Baltscheffsky, M. & Baltscheffsky, H. H^+-PPases: yesterday, today and tomorrow. *IUBMB Life* **59**, 76-83 (2007). https://doi.org/10.1080/15216540701258132

6 Kajander, T., Kellosalo, J. & Goldman, A. Inorganic pyrophosphatases: one substrate, three mechanisms. *FEBS Lett.* **587**, 1863-1869 (2013). https://doi.org/10.1016/j.febslet.2013.05.003

7 Jannik, S. *et al.* Functional and structural asymmetry suggest a unifying principle for catalysis in integral membrane-bound pyrophosphatases. *EMBO Reports*, 853-875 (2023).

8 Kellosalo, J., Kajander, T., Kogan, K., Pokharel, K. & Goldman, A. The Structure and Catalytic Cycle of a Sodium-Pumping Pyrophosphatase. *Science* **337**, 473-476 (2012). https://doi.org/10.1126/science.1222505

9 Li, K.-M. *et al.* Membrane pyrophosphatases from *Thermotoga maritima* and *Vigna radiata* suggest a conserved coupling mechanism. *Nat. Comm.* **7**, 13596 (2016). https://doi.org/10.1038/ncomms13596

10 Vidilaseris, K. *et al.* Asymmetry in catalysis by *Thermotoga maritima* membrane-bound pyrophosphatase demonstrated by a nonphosphorus allosteric inhibitor. *Science Advances* **5**, eaav7574 (2019). https://doi.org/10.1126/sciadv.aav7574

11 Lin, S.-M. *et al.* Crystal structure of a membrane-embedded H+-translocating pyrophosphatase. *Nature* **484**, 399-403 (2012). https://doi.org/10.1038/nature10963

12 Tsai, J. Y. *et al.* Roles of the Hydrophobic Gate and Exit Channel in Vigna radiata Pyrophosphatase Ion Translocation. *J. Mol. Biol.* **431**, 1619-1632 (2019). https://doi.org/10.1016/j.jmb.2019.03.009

13 Tsai, J.-Y., Kellosalo, J., Sun, Y.-J. & Goldman, A. Proton/sodium pumping pyrophosphatases: the last of the primary ion pumps. *Curr. Opin. Struct. Biol.* **27**, 38-47 (2014). https://doi.org/10.1016/j.sbi.2014.03.007

14 Ballesteros, J. A. & Weinstein, H. in *Methods in Neurosciences* Vol. 25 (ed Stuart C. Sealfon) 366-428 (Academic Press, 1995).

15 Tsai, J.-Y., Kellosalo, J., Sun, Y.-J. & Goldman, A. Proton/sodium pumping pyrophosphatases: the last of the primary ion pumps. *Current Opinion in Structural Biology* **27**, 38-47 (2014). https://doi.org/https://doi.org/10.1016/j.sbi.2014.03.007

16 Johansson, N. G. *et al.* Exploration of Pyrazolo[1,5‐a]pyrimidines as Membrane‐Bound Pyrophosphatase Inhibitors. *ChemMedChem* (2021). https://doi.org/10.1002/cmdc.202100392

17 Johansson, N. G. *et al.* Discovery of Membrane-Bound Pyrophosphatase Inhibitors Derived from an Isoxazole Fragment. *ACS Med. Chem. Lett.* **11**, 605-610 (2020). https://doi.org/10.1021/acsmedchemlett.9b00537

18 Shah, N. R., Vidilaseris, K., Xhaard, H. & Goldman, A. Integral membrane pyrophosphatases: a novel drug target for human pathogens? *AIMS Biophysics* **3**, 171-194 (2016). https://doi.org/10.3934/biophy.2016.1.171

19 Vidilaseris, K. *et al.* Screening for Thermotoga maritima Membrane-Bound Pyrophosphatase Inhibitors. *JoVE*, e60619 (2019). https://doi.org/doi:10.3791/60619

20 Vidilaseris, K. *et al.* Asymmetry in catalysis by Thermotoga maritima membrane-bound pyrophosphatase demonstrated by a nonphosphorus allosteric inhibitor. *Sci. Adv* **5**, 12 (2019). https://doi.org/10.1126/sciadv.aav7574

21 Artukka, E., Luoto, H. H., Baykov, A. A., Lahti, R. & Malinen, A. M. Role of the potassium/lysine cationic center in catalysis and functional asymmetry in membrane-bound pyrophosphatases. *Biochem. J.* **475**, 1141-1158 (2018). https://doi.org/10.1042/BCJ20180071

22 Anashkin, V. A., Malinen, A. M., Bogachev, A. V. & Baykov, A. A. Catalytic Asymmetry in Homodimeric H+-Pumping Membrane Pyrophosphatase Demonstrated by Non-Hydrolyzable Pyrophosphate Analogs. *International Journal of Molecular Sciences* **22** (2021). https://doi.org/10.3390/ijms22189820

23 Drake, M. T., Clarke, B. L. & Khosla, S. Bisphosphonates: mechanism of action and role in clinical practice. *Mayo Clin. Proc.* **83**, 1032-1045 (2008). https://doi.org/10.4065/83.9.1032

24 Jeschke, G. The contribution of modern EPR to structural biology. *Emerging Topics in Life Sciences* **2**, 9-18 (2018).

25 Schiemann, O. & Prisner, T. F. Long-range distance determinations in biomacromolecules by EPR spectroscopy. *Q Rev Biophys* **40**, 1-53 (2007). https://doi.org/10.1017/s003358350700460x

26 Goldfarb, D. Exploring protein conformations in vitro and in cell with EPR distance measurements. *Curr Opin Struct Biol* **75**, 102398 (2022). https://doi.org/10.1016/j.sbi.2022.102398

27 McHaourab, Hassane S., Steed, P. R. & Kazmier, K. Toward the Fourth Dimension of Membrane Protein Structure: Insight into Dynamics from Spin-Labeling EPR Spectroscopy. *Structure* **19**, 1549-1561 (2011). https://doi.org/https://doi.org/10.1016/j.str.2011.10.009

28 Bordignon, E., Kucher, S. & Polyhach, Y. in *Lipid-Protein Interactions: Methods and Protocols* (ed Jörg H. Kleinschmidt) 493-528 (Springer New York, 2019).

29 Hartley, A. M., Ma, Y., Lane, B. J., Wang, B. & Pliotas, C. in *Electron Paramagnetic Resonance: Volume 27* Vol. 27 74-108 (The Royal Society of Chemistry, 2020).

30 Pliotas, C. *et al.* Conformational state of the MscS mechanosensitive channel in solution revealed by pulsed electron–electron double resonance (PELDOR) spectroscopy. *Proceedings of the National Academy of Sciences* **109**, E2675-E2682 (2012). https://doi.org/10.1073/pnas.1202286109

31 Kapsalis, C. *et al.* Allosteric activation of an ion channel triggered by modification of mechanosensitive nano-pockets. *Nature Communications* **10**, 4619 (2019). https://doi.org/10.1038/s41467-019-12591-x

32 Haysom, S. F. *et al.* Inside Cover: Darobactin B Stabilises a Lateral-Closed Conformation of the BAM Complex in E. coli Cells (Angew. Chem. Int. Ed. 34/2023). *Angewandte Chemie International Edition* **62**, e202308371 (2023). https://doi.org/https://doi.org/10.1002/anie.202308371

33 Kapsalis, C., Ma, Y., Bode, B. E. & Pliotas, C. In-Lipid Structure of Pressure-Sensitive Domains Hints Mechanosensitive Channel Functional Diversity. *Biophysical Journal* **119**, 448-459 (2020). https://doi.org/https://doi.org/10.1016/j.bpj.2020.06.012

34 Gopinath, A., Rath, T., Morgner, N. & Joseph, B. Lateral gating mechanism and plasticity of the β-barrel assembly machinery complex in micelles and Escherichia coli. *PNAS Nexus* **3**, pgae019 (2024). https://doi.org/10.1093/pnasnexus/pgae019

35 Galazzo, L. *et al.* The ABC transporter MsbA adopts the wide inward-open conformation in E. coli cells. *Sci. Adv.* **8**, eabn6845 https://doi.org/10.1126/sciadv.abn6845

36 Thaker, T. M. *et al.* Asymmetric drug binding in an ATP-loaded inward-facing state of an ABC transporter. *Nature Chemical Biology* **18**, 226-235 (2022). https://doi.org/10.1038/s41589-021-00936-x

37 Wingler, L. M. *et al.* Angiotensin Analogs with Divergent Bias Stabilize Distinct Receptor Conformations. *Cell* **176**, 468-478.e411 (2019). https://doi.org/10.1016/j.cell.2018.12.005

38 Beck, M., Covino, R., Hänelt, I. & Müller-McNicoll, M. Understanding the cell: Future views of structural biology. *Cell* **187**, 545-562 (2024). https://doi.org/10.1016/j.cell.2023.12.017

39 Lane, B. J. *et al.* Monitoring the conformational ensemble and lipid environment of a mechanosensitive channel under cyclodextrin-induced membrane tension. *Structure* (2024). https://doi.org/https://doi.org/10.1016/j.str.2024.02.020

40 Zhao, J. *et al.* Ligand efficacy modulates conformational dynamics of the μ-opioid receptor. *Nature* **629**, 474-480 (2024). https://doi.org/10.1038/s41586-024-07295-2

41 Gordon-Weeks, R., Parmar, S., Davies, T. G. E. & Leigh, R. A. Structural aspects of the effectiveness of bisphosphonates as competitive inhibitors of the plant vacuolar proton-pumping pyrophosphatase. *Biochemical Journal* **337**, 373-377 (1999). https://doi.org/10.1042/bj3370373

42 Vidilaseris, K. *et al.* Screening for Thermotoga maritima Membrane-Bound Pyrophosphatase Inhibitors. *Journal of Visual Experiment* (2019). https://doi.org/10.3791/60619

43 Yamagata, S. & Iwama, T. Determination of a Small Quantity of Cystine in the Presence of a Large Amount of Cysteine. *Biosci Biotechnol Biochem* **63**, 1503-1505 (1999). https://doi.org/10.1271/bbb.63.1503

44 Tickle, I. *et al.* Staraniso. *Global Phasing Ltd., Cambridge, UK* (2016).

45 Li, K.-M. *et al.* Membrane pyrophosphatases from Thermotoga maritima and Vigna radiata suggest a conserved coupling mechanism. *Nat. Commun.* **7**, 13596 (2016). https://doi.org/10.1038/ncomms13596

46 Dahl, A. C., Chavent, M. & Sansom, M. S. Bendix: intuitive helix geometry analysis and abstraction. *Bioinformatics* **28**, 2193-2194 (2012). https://doi.org/10.1093/bioinformatics/bts357

47 Branigan, E., Pliotas, C., Hagelueken, G. & Naismith, J. H. Quantification of free cysteines in membrane and soluble proteins using a fluorescent dye and thermal unfolding. *Nature protocols* **8**, 2090-2097 (2013).

48 Lane, B. J. *et al.* HDX-guided EPR spectroscopy to interrogate membrane protein dynamics. *STAR Protocols* **3**, 101562 (2022). https://doi.org/https://doi.org/10.1016/j.xpro.2022.101562

49 Pliotas, C. Ion Channel Conformation and Oligomerization Assessment by Site-Directed Spin Labeling and Pulsed-EPR. *Methods Enzymol* **594**, 203-242 (2017). https://doi.org/10.1016/bs.mie.2017.05.013

50 Hagelueken, G., Ward, R., Naismith, J. H. & Schiemann, O. MtsslWizard: In Silico Spin-Labeling and Generation of Distance Distributions in PyMOL. *Appl Magn Reson* **42**, 377-391 (2012). https://doi.org/10.1007/s00723-012-0314-0

51 Song, Y. *et al.* High-resolution comparative modeling with RosettaCM. *Structure* **21**, 1735-1742 (2013). https://doi.org/10.1016/j.str.2013.08.005

52 Bazzone, A., Barthmes, M. & Fendler, K. in *Methods in Enzymology* Vol. 594 (ed Christine Ziegler) 31-83 (Academic Press, 2017).

53 Malinen, A. M. *et al.* Pre-steady-state kinetics and solvent isotope effects support the "billiard-type" transport mechanism in Na+-translocating pyrophosphatase. *Protein Science* **31**, e4394 (2022). https://doi.org/https://doi.org/10.1002/pro.4394

54 Kellosalo, J., Kajander, T., Palmgren, M. G., Lopez-Marques, R. L. & Goldman, A. Heterologous expression and purification of membrane-bound pyrophosphatases. *Protein Expr. Purif.* **79**, 25-34 (2011). https://doi.org/10.1016/j.pep.2011.05.020

55 López-Marqués, R. L. *et al.* Large-scale purification of the proton pumping pyrophosphatase from *Thermotoga maritima*: A "Hot-Solve" method for isolation of recombinant thermophilic membrane proteins. *Biochim. Biophys. Acta* **1716**, 69-76 (2005). https://doi.org/10.1016/j.bbamem.2005.08.004

56 Kellosalo, J., Kajander, T., Kogan, K., Pokharel, K. & Goldman, A. The structure and catalytic cycle of a sodium-pumping pyrophosphatase. *Science* **337**, 473-476 (2012). https://doi.org/10.1126/science.1222505

57 Vidilaseris, K., Kellosalo, J. & Goldman, A. A high-throughput method for orthophosphate determination of thermostable membrane-bound pyrophosphatase activity. *Analytical Methods* **10**, 646-651 (2018). https://doi.org/10.1039/C7AY02558K

58 Kabsch, W. XDS. *Acta Crystallogr. D: Biol. Crystallogr.* **66**, 125-132 (2010). https://doi.org/10.1107/S0907444909047337

59 McCoy, A. J. *et al.* Phaser crystallographic software. *J. Appl. Crystallogr.* **40**, 658-674 (2007). https://doi.org/10.1107/S0021889807021206

60 Adams, P. D. *et al.* PHENIX: a comprehensive Python-based system for macromolecular structure solution. *Acta Cryst. Sect. D: Biol. Crystallogr.* **66**, 213-221 (2010). https://doi.org/10.1107/S0907444909052925

61 Emsley, P., Lohkamp, B., Scott, W. G. & Cowtan, K. Features and development of Coot. *Acta Cryst. Sect. D: Biol. Crystallogr.* **66**, 486-501 (2010). https://doi.org/10.1107/S0907444910007493

62 Hubbell, W. L., Gross, A., Langen, R. & Lietzow, M. A. Recent advances in site-directed spin labeling of proteins. *Current opinion in structural biology* **8**, 649-656 (1998).

63 Jeschke, G. DEER Distance Measurements on Proteins. *Annual Review of Physical Chemistry* **63**, 419-446 (2012). https://doi.org/https://doi.org/10.1146/annurev-physchem-032511-143716

64 Milov, A., Ponomarev, A. & Tsvetkov, Y. D. Electron-electron double resonance in electron spin echo: Model biradical systems and the sensitized photolysis of decalin. *Chem. Phys. Lett.* **110**, 67-72 (1984).

65 Tait, C. E. & Stoll, S. Coherent pump pulses in Double Electron Electron Resonance spectroscopy. *Phys. Chem. Chem. Phys.* **18**, 18470-18485 (2016). https://doi.org/10.1039/c6cp03555h

66 Russell, H., Cura, R. & Lovett, J. E. DEER Data Analysis Software: A Comparative Guide. *Frontiers in Molecular Biosciences* **9** (2022). https://doi.org/10.3389/fmolb.2022.915167

67 Schiemann, O. *et al.* Benchmark Test and Guidelines for DEER/PELDOR Experiments on Nitroxide-Labeled Biomolecules. *Journal of the American Chemical Society* **143**, 17875-17890 (2021). https://doi.org/10.1021/jacs.1c07371

68 Teucher, M. & Bordignon, E. Improved signal fidelity in 4-pulse DEER with Gaussian pulses. *Journal of Magnetic Resonance* **296**, 103-111 (2018). https://doi.org/https://doi.org/10.1016/j.jmr.2018.09.003

69 Chiang, Y. W., Borbat, P. P. & Freed, J. H. The determination of pair distance distributions by pulsed ESR using Tikhonov regularization. *J Magn Reson* **172**, 279-295 (2005). https://doi.org/10.1016/j.jmr.2004.10.012

70 Jeschke, G. *et al.* DeerAnalysis2006—a comprehensive software package for analyzing pulsed ELDOR data. *Applied Magnetic Resonance* **30**, 473-498 (2006). https://doi.org/10.1007/BF03166213

Figure legends

Figure 1. **Inhibition effect of bisphosphonates on TmPPase.**

A. Overall structure of the monomer TmPPase structure, consisting of hydrolytic centre, coupling funnel, ion gate and exit channel. **B**. Chemical structure of IDP and bisphosphonates and their inhibition activity against TmPPase. **C**. Activity of TmPPase modified with NEM (N-Ethylmaleimide) in the presence of $MgCl_2$ (2.5 mM) and NaCl (20 mM) after incubation with Ca^{2+} (2 mM) and bisphosphonates (0.5 mM). Measurement was done in triplicate.

Figure 2. Structural asymmetry in the dimer active-site of TmPPase:ETD complex.

A. Superposition of chain A (cyan) and chain B (wheat) showing the relative movements (black arrow) of helices. **B**. Superposition of TMH5 and TMH6 in TmPPase:ETDs and TmPPase:IDP (orange; PDB: 5LZQ) showing the movement of loop5-6 and reorientation of ETD_A, ETD_B and IDP. The dashed line shows the interaction of $E217^{5.76}$ of loop5-6 in Chain A with ETD_A and IDP, and $D218^{5.77}$ of loop5-6 in Chain B with ETD_B.; Close-up view of IDP superposed with ETD_A and ETD_B. **C**. Residues in the active site with ETD_A coordinated (dashed lines), Ca^{2+} (pink sphere) and nucleophilic water (red spheres) in a Mg^{2+} metal cage (green spheres). **D**. Residues in active site with ETD_B coordinated (dashed lines), Ca^{2+} (pink sphere) and water (red spheres) in a Mg^{2+} metal cage (green spheres).

Figure 3. **Comparison of the TmPPase:ZLD and TmPPase:IDP structures in the active site.**

A. Superposition of TmPPase:ZLD (chain A, pink) and TmPPase: IDP (chain A, orange) (PDB: 5LZQ). Helices movements are indicated by a black arrow. **B** Cross-section view of the active site in TmPPase:ZLD. **C**. Cross-section view of the active site in TmPPase:IDP. **D**. Superposition of TMH11, TMH12 and TMH15 in TmPPase:ZLD and TmPPase:IDP showed the movement of the hydrolytic centre and the orientation of ZLD and IDP. **E**. The coordination of key residues in the active site with ZLD (dash line), and water (red sphere) in a Mg^{2+} metal cage (green spheres). **F**. The coordination of key residues in the active site with IDP (dash line) in a Mg^{2+} metal cage (green spheres).

Figure 4. DEER distance distributions of TmPPase S525R1 under different conditions.

A. Structure of the TmPPase dimer, with monomers A and B coloured cyan and purple, respectively. The sites mutated to cysteine and labelled with MTSSL are shown by maroon spheres, with T211R1 on

the cytoplasmic (top) side and S525R1 on the periplasmic (bottom) side of the membrane. **B.** DEER raw data traces for S525R1. Each condition measured is coloured accordingly. **C.** DEER background corrected time-domain traces for S525R1. The black dashed line represents the base of the oscillation in the *apo* state and acts as a guide to highlight the small distance changes where the base of the oscillation comes before (shorter distance) or after (longer distance) the line. **D.** The overlap between the predicted distance distribution of S525R1 from the solved crystal structures (TmPPase:Ca, TmPPase:Ca:ETD, TmPPase:ZLD, and TmPPase:IDP), shown as coloured dashed lines, with the resulting DEER distance distributions at the respective conditions. The vertical black dashed line represents the mean distance for the *apo* state to highlight changes from this to shorter and longer distances. The grey-shaded regions represent the uncertainty in the distribution and the coloured bar above the x-axis represents the DeerAnalysis 'traffic light' system for assessing the reliability of the distribution presented. For the time window of this dataset, the distances within the regions highlighted in green and yellow indicate the reliability of the mean distance, peak shape, and width. For distance peaks within the orange region (> 5.0 nm), only the mean distance is considered reliable[70]. The data were all processed in DeerAnalysis, with validation in the same way as described in the methods.

Figure 5. Combinded model of Ca (monomer A) and IDP (monomer B) structures

A. Side and bottom views of the symmetric and asymmetric structures for IDP bound to TmPPase. The asymmetric model combines a monomer (A) of TmPPase_Ca and a monomer (B) of TmPPase_IDP. **B.** The overlap of their predicted distance distribution and resulting experimental DEER distance distribution for S525R1.

Figure 6. **Transient currents of TmPPase Na^+ pumping and ion gate of TmPPase structures.**

A. Curve of Na^+ pumping current triggered by 100 µM of K_4PP_i, 50 µM of IDP, 50 µM of ETD, 50 µM of ZLD, and 200 µM of K_2HPO_4. The vertical black dased line represents the addition of activating buffer and non-activating buffer. **C-E**. Ion gate of TmPPase:Ca (yellow); TmPPase:ETD (cyan); TmPPase:ZLD (green); TmPPase:IDP (purple). The black arrows show the movement of residues of D703[16.46] and K707[16.50].

Figure 7. **Models** based on **DEER distance distributions for TmPPase S525R1 and T211R1.**

Five DEER models of PfPPase bound bisphosnates. TMH12, 13 and loop12-13 are shown in brown; TMH5, 6 and loop5-6 are shown in green. The labelling sites are represented by maroon spheres.

Within the structures, Ca^{2+} is shown as a green circle; ETD by a purple square; ZLD by an orange pentagon and IDP as blue square.

Expanded View Figure legends

Figure EV1. Inhibition of TmPPase by bisphosphonates. All data are shown as mean ± SD with three replicates.

Figure EV2. **Accessible cystines for NEM modification.**

A. Two exposed cysteines in both monomers of TmPPase:Ca (PDB: 4AV3; cyan). **B**. One exposed cystine in both monomers of TmPPase:IDP (PDB: 5LZQ; wheat).

Figure EV3. Electron density maps of ETD at the active sites.

A. mF_o– F_c omit map with positive density of the ETD_A shown in green mesh (*Top left*); Polder omit map of ETD_A (*Bottom left*) shown in yellow mesh; $2mF_o$–F_c (blue mesh) map of ETD_A, ions and surrounding residues (*Right*). **B**. mF_o– F_c omit map with positive density of the ETD_B shown in green mesh (*Top left*); Polder omit map of ETD_B (*Bottom left*) shown in yellow mesh; $2mF_o$–F_c (blue mesh) map of ETD_B, ions and surrounding residues (*Right*). Ca^{2+} ion is shown in purple; Mg^{2+} ions are shown in green and water molecules are shown in red.

Figure EV4. Electron density maps of ZLD at the active sites. . **A.** mF_o– F_c omit map with positive density of the ZLD_A shown in green mesh (*Top left*); Polder omit map of ZLD_A (*Bottom left*) shown in yellow mesh; $2mF_o$–F_c (blue mesh) map of ZLD_A, ions and surrounding residues (*Right*). **B**. mF_o– F_c omit map with positive density of the ZLD_B shown in green mesh (*Top left*); Polder omit map of ZLD_B (*Bottom left*) shown in yellow mesh; $2mF_o$–F_c (blue mesh) map of ZLD_B, ions and surrounding residues (*Right*). **C.** mF_o– F_c omit map with positive density of the ZLD_C shown in green mesh (*Top left*); Polder omit map of ZLD_C (*Bottom left*) shown in yellow mesh; $2mF_o$–F_c (blue mesh) map of ZLD_C, ions and surrounding residues (*Right*). **D**. mF_o– F_c omit map with positive density of the ZLD_D shown in green mesh (*Top left*); Polder omit map of ZLD_D (*Bottom left*) shown in yellow mesh; $2mF_o$–F_c (blue mesh) map of ZLD_D, ions and surrounding residues (*Right*).

Figure EV5. Electron density maps of loop5-6 in the TmPPase:ETD structure.

A. $2mF_o–F_c$ (blue mesh) electron density map of loop5-6 at chain A. **B**. $2mF_o–F_c$ (blue mesh) electron density map of loop5-6 at chain B.

Figure EV6. **Helix curvature comparison between chain A and chain B of the TmPPase:ETD structure**.

Changes in helix curvature are shown in the hydrolytic side of TMH11, TMH12, and TMH15. The black bar shows the region in the hydrolytic centre side.

Figure EV7. Ion gates of TmPPase structures.

A. Superposition of the ion gate of the four TmPPase structures (yellow: TmPPase:Ca; cyan: TmPPase:ETD; green: TmPPase:ZLD; purple: TmPPase:IDP; Na^+ is shown as a purple sphere). The movement of TMH16 is shown as the black arrow. **B-C.** The 2mFo-Fc and mFo-Fc density map of ion gate in the TmPPase:ETD (cyan) and TmPPase:ZLD (green) structure.

Figure EV8. DEER distance distributions of TmPPase T211R1 under different conditions.

A. Structure of the TmPPase dimer (PDB: 5LZQ), with monomers A and B coloured cyan and purple, respectively. The sites that were mutated to cysteine and labelled with MTSSL are shown by maroon spheres, with T211R1 on the cytoplasmic (top) side and S525R1 on the periplasmic (bottom) side of the membrane interface. **B.** DEER raw data traces for T211R1. Each condition measured is coloured according to the condition used. **C.** DEER background-corrected time-domain traces for T211R1. **D.** The overlap between the predicted distance distribution of T211R1 from the solved crystal structures (TmPPase:Ca, TmPPase:Ca:ETD, TmPPase:ZLD, and TmPPase:IDP), shown as dashed lines, with the resulting DEER distance distributions at the respective conditions. The grey-shaded regions represent the uncertainty in the distribution. The data were all processed in DeerAnalysis, with validation in the same way as described in the methods.

Figure EV9. CW EPR spectra of TmPPase T211R1 and S525R1 under different conditions. The CW EPR data were collected at room temperature before the addition of ethylene glycol and therefore represent the rotational motion of the spin labels in comparison to each other. **A.** The normalized CW EPR data for T211R1 in its *apo* form, and with ETD and IDP added. **B.** The normalized CW EPR data for S525R1 for *apo*, +Ca(II), +Ca/ETD and +ETD conditions.

Figure EV10. ComparativeDeerAnalyzer (CDA) data of TmPPase S525R1 and T211R1.

A. The background-corrected data and distance distributions for S525R1 generated by the automated CDA software. **B.** The background-corrected data and distance distributions for T211R1 generated by the automated CDA software.

Supplementary Tables

Table S1. X-ray data collection and refinement statistics.

Data Parameters	TmPPase+Etidronate	TmPPase+Zoledronate
Crystallisation condition	0.2M CaCl2, 0.1M HEPES pH 7.0, 33% PEG 400	0.1M NaCl, 0.1M MES pH 6.5, 33% PEG 400, 4% ethylene glycol
Space group	P 2_1	P $2_12_12_1$
Cell dimensions		
a, b, c (Å)	83.7, 111.7, 105.2	101.188, 147.366, 252.341
α, β, γ (°)	90.0, 106.7, 90.0	90.0, 90.0, 90.0
Source	DLS I03	DLS I04-1
Wavelength (Å)	0.91587	0.97625
Resolution (Å)	80.2 - 3.15 (3.56 - 3.15)	127.3 - 3.26 (3.31 - 3.26)
Overall (Å)	3.15	3.26
along h axis	3.10	4.46
along k axis	3.60	4.17
along l axis	4.31	3.17
Measured reflections	130818	445655
Unique reflections	19273	33220
Completeness (%)	91.6 (59.3)	93.7 (72.2)
$CC_{1/2}$	0.999 (0.494)	0.999 (0.573)
Mean I/σ(I)	9.7 (1.6)	10.2 (1.7)
Multiplicity	6.8 (7.0)	13.4 (12.2)
Wilson B (Å^2)	98.7	118.03
R_{merge}	0.098 (1.193)	0.137 (1.785)
R_{meas}	0.106 (1.29)	0.143 (1.860)
Rpim	0.041 (0.486)	0.039 (0.516)

Refinement		
Resolution (Å)	74.81 - 3.15 (3.27 - 3.15)	48.22 - 3.27 (3.39 - 3.27)
R_{work}(%)/R_{free}(%)	27.2/31.0	25.9/30.4
No. of atoms	10043	20790
protein	10003	20704
ligands	44	104
water	8	6
No. of chains (ASU)	2	4
B-factors (Å2)	88.96	106.62
Protein	88.85	106.53
Ligands/Ion	127.07	133.77
R.m.s. deviations		
Bond lengths (Å)	0.003	0.005
Bond angle (°)	0.63	0.76
Ramachandran statistics[†]		
Favoured (%)	97.73	98.59
Allowed (%)	2.27	1.41
Outliers (%)	0.00	0.00

Table S2. Structural alignments between chains of different TmPPase structures

Chain	**ETD_A:ETD_B**	**$4AV3_A$:$4AV3_B$**	**ETD_A:$4AV3_A$**	**ETD_B:$4AV3_B$**	**ETD_A:$4AV3_B$**	**ETD_B:$4AV3_A$**
C_α RMSD (Å)	1.44	0.39	0.72	0.94	0.70	0.98
Chain	**ZLD_A:ZLD_B**	**$5LZQ_A$:$5LZQ_B$**	**ZLD_A:$5LZQ_A$**	**ZLD_B:$5LZQ_B$**	**ZLD_A: $5LZQ_B$**	**ZLD_B:$5LZQ_A$**
C_α RMSD (Å)	0.51	0.21	0.72	0.72	0.74	0.69
Chain	**ZLD_A:ZLD_C**	**ZLD_A:ZLD_D**	**ZLD_C:ZLD_D**	**ZLD_B:ZLD_D**	**ZLD_B:ZLD_C**	
C_α RMSD (Å)	0.58	0.68	0.90	0.61	0.66	

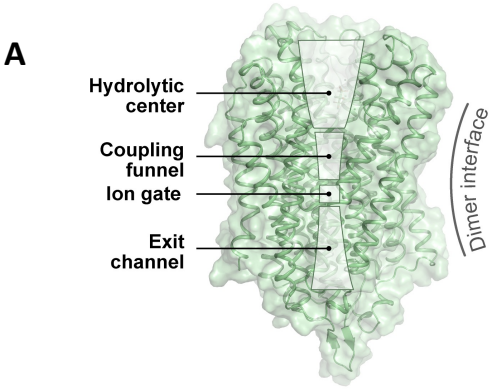
A
Hydrolytic center
Coupling funnel
Ion gate
Exit channel
Dimer interface

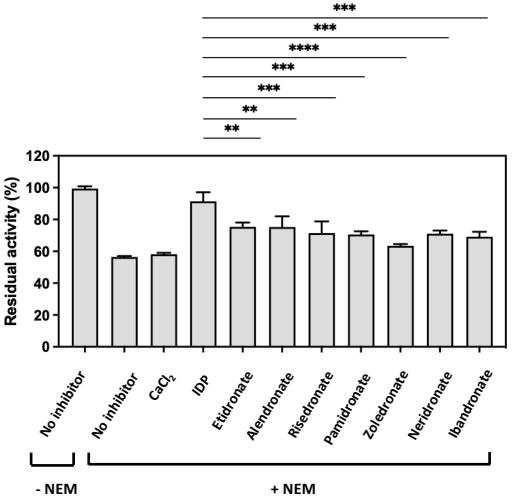
C
***
***
****
***
***
**
**
Residual activity (%)
120
100
80
60
40
20
0
No inhibitor
No inhibitor
CaCl2
IDP
Etidronate
Alendronate
Risedronate
Pamidronate
Zoledronate
Neridronate
Ibandronate
- NEM
+ NEM

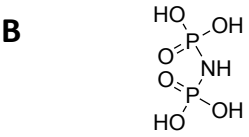
B
Imidodiphosphate
IC50= 56.4 ± 5.4 μM

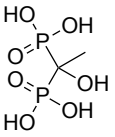
Etidronate
IC50 > 200 μM

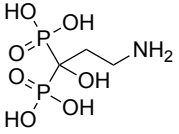
Pamidronate
IC50= 119 ± 7.4 μM

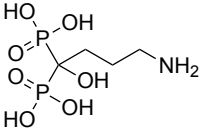
Alendronate
IC50= 118 ± 12.5 μM

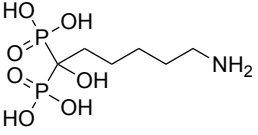
Neridronate
IC50= 138 ± 8.8 μM

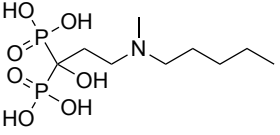
Ibandronate
IC50 > 200 μM

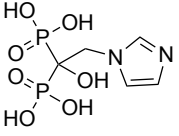
Zoledronate
IC50 > 200 μM

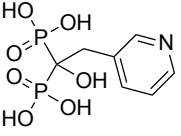
Risedronate
IC50 > 200 μM

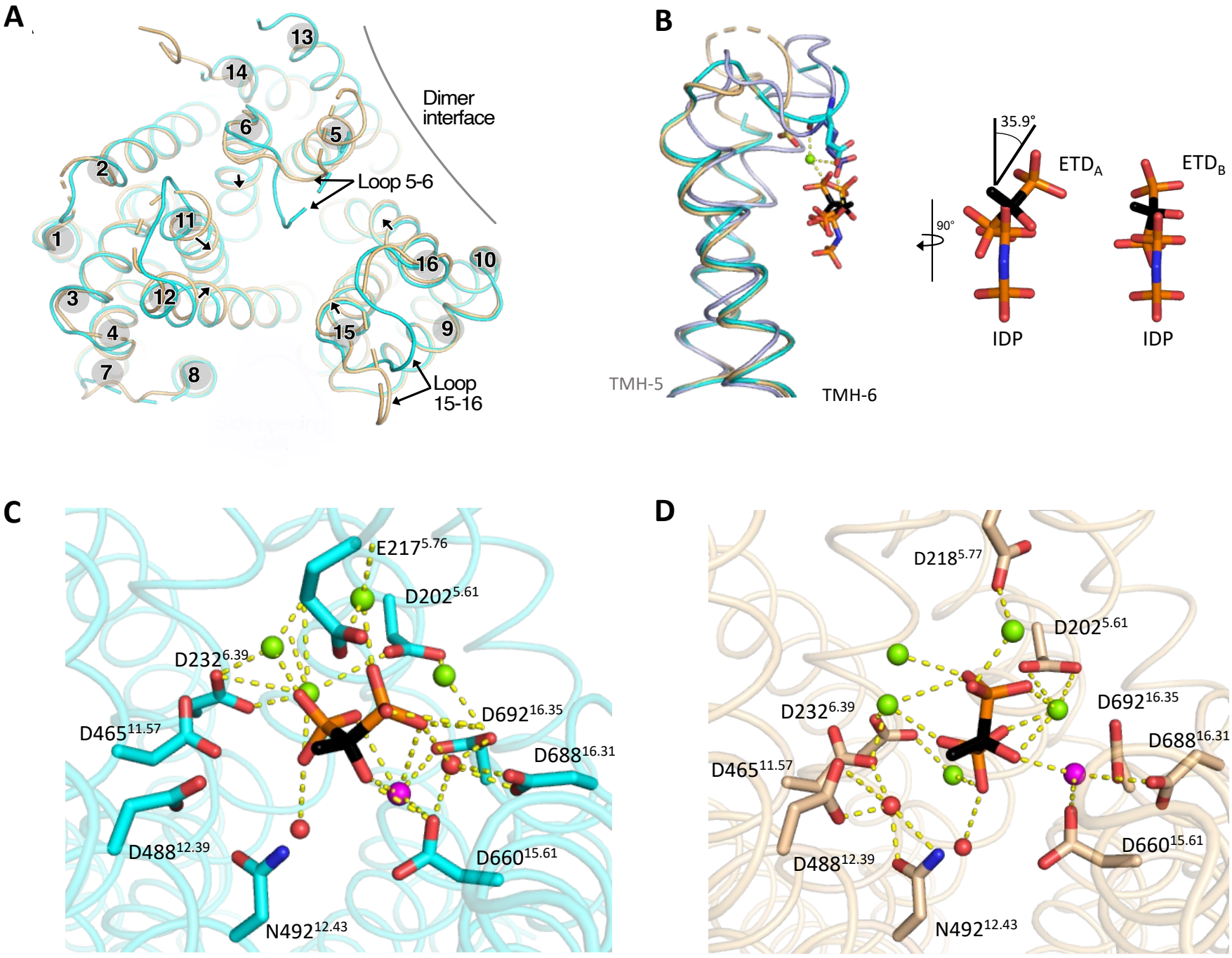
A
13
14
6
5
2
1
11
3
12
4
7
8
16
10
15
9
Dimer interface
Loop 5-6
Loop 15-16
B
TMH-5
TMH-6
35.9°
90°
ETD$_A$
ETD$_B$
IDP
IDP
C
E217$^{5.76}$
D202$^{5.61}$
D232$^{6.39}$
D465$^{11.57}$
D692$^{16.35}$
D688$^{16.31}$
D488$^{12.39}$
D660$^{15.61}$
N492$^{12.43}$
D
D218$^{5.77}$
D202$^{5.61}$
D232$^{6.39}$
D692$^{16.35}$
D688$^{16.31}$
D465$^{11.57}$
D660$^{15.61}$
D488$^{12.39}$
N492$^{12.43}$

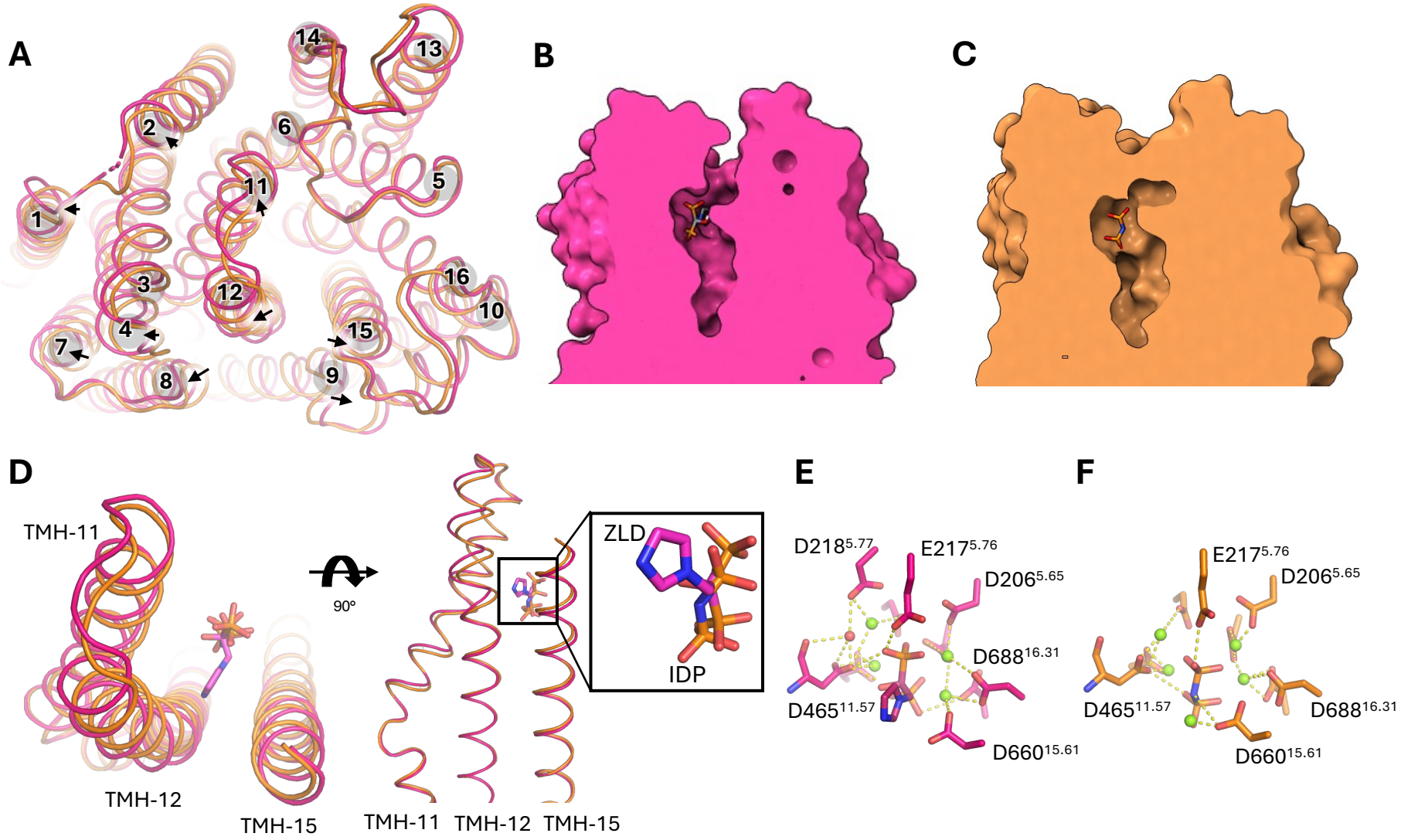
A
1
2
3
4
5
6
7
8
9
10
11
12
13
14
15
16
B
C
D
TMH-11
TMH-12
TMH-15
90°
TMH-11
TMH-12
TMH-15
ZLD
IDP
E
D218$^{5.77}$
E217$^{5.76}$
D206$^{5.65}$
D688$^{16.31}$
D465$^{11.57}$
D660$^{15.61}$
F
E217$^{5.76}$
D206$^{5.65}$
D465$^{11.57}$
D688$^{16.31}$
D660$^{15.61}$

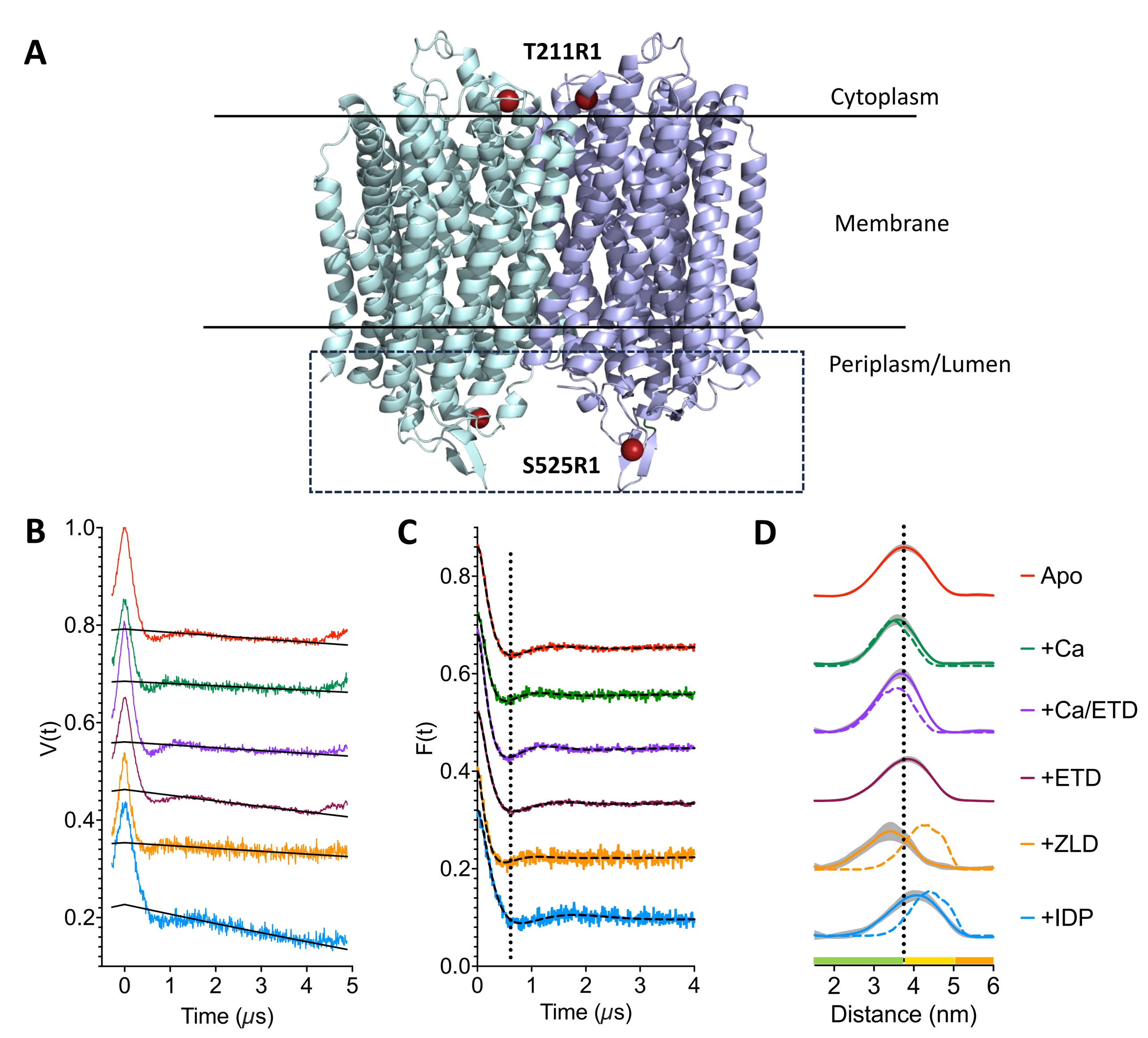
A
T211R1
Cytoplasm
Membrane
Periplasm/Lumen
S525R1
B
V(t)
Time (μs)
C
F(t)
Time (μs)
D
Distance (nm)
Apo
+Ca
+Ca/ETD
+ETD
+ZLD
+IDP

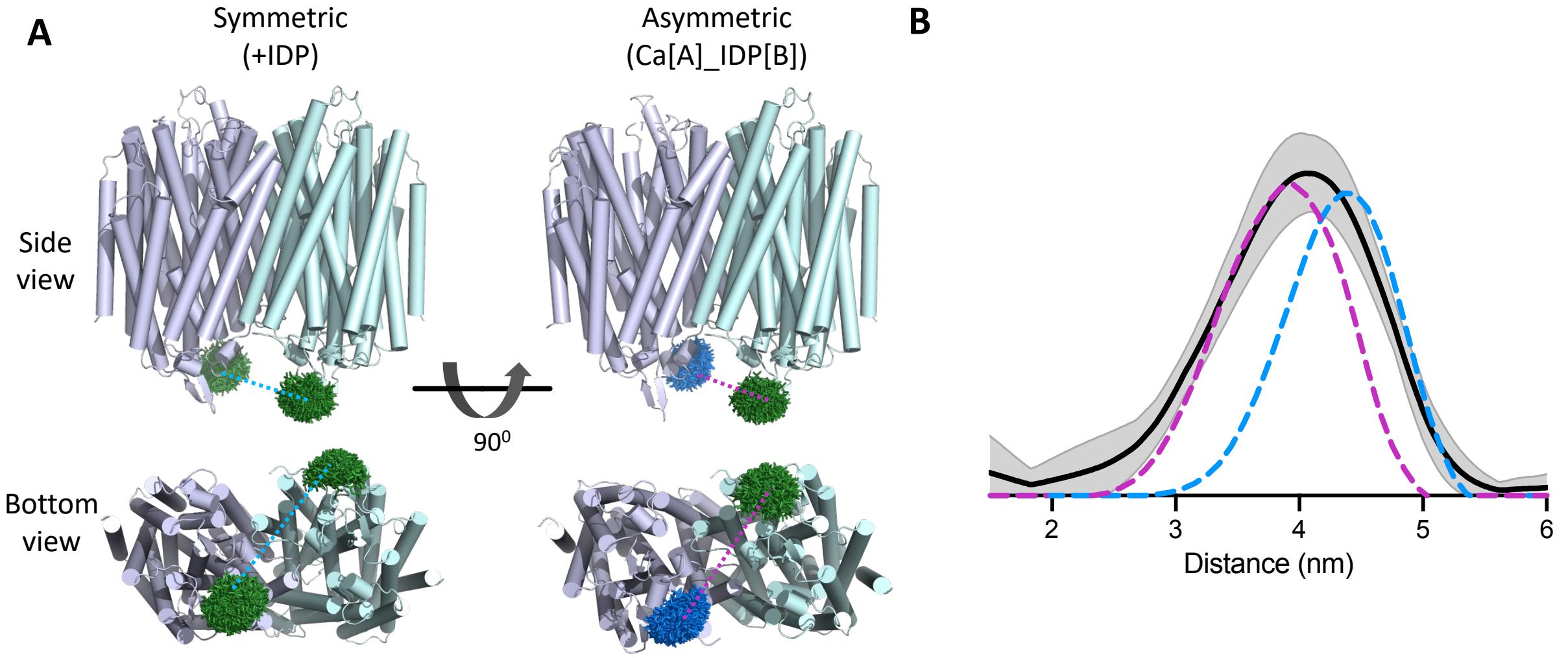
A
Symmetric
(+IDP)
Asymmetric
(Ca[A]_IDP[B])
Side
view
90⁰
Bottom
view
B
2
3
4
5
6
Distance (nm)

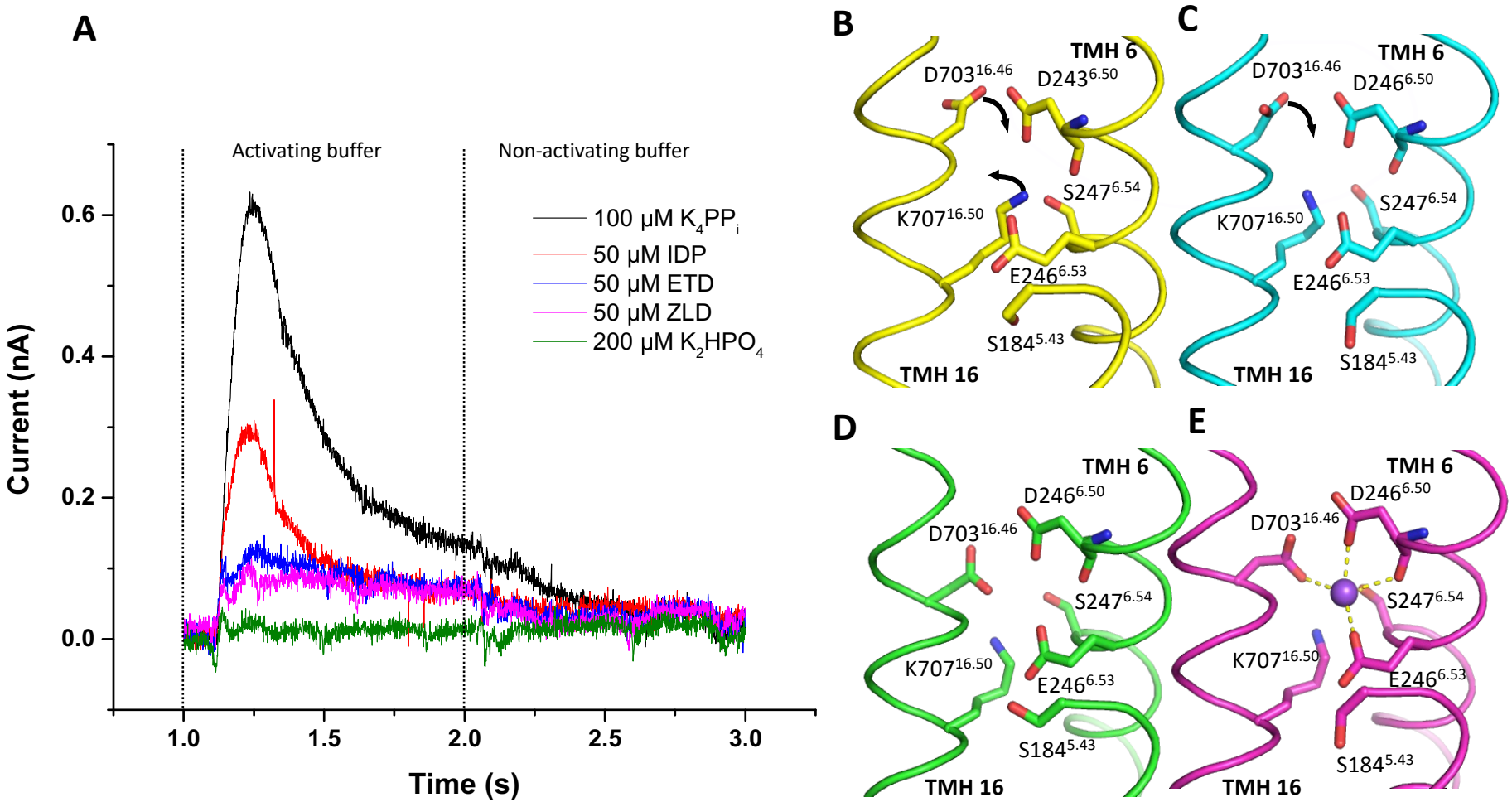
A
Activating buffer
Non-activating buffer
100 μM K_4PP_i
50 μM IDP
50 μM ETD
50 μM ZLD
200 μM K_2HPO_4
Current (nA)
0.6
0.4
0.2
0.0
1.0
1.5
2.0
2.5
3.0
Time (s)
B
TMH 6
$D703^{16.46}$
$D243^{6.50}$
$S247^{6.54}$
$K707^{16.50}$
$E246^{6.53}$
$S184^{5.43}$
TMH 16
C
TMH 6
$D703^{16.46}$
$D246^{6.50}$
$S247^{6.54}$
$K707^{16.50}$
$E246^{6.53}$
$S184^{5.43}$
TMH 16
D
TMH 6
$D246^{6.50}$
$D703^{16.46}$
$S247^{6.54}$
$K707^{16.50}$
$E246^{6.53}$
$S184^{5.43}$
TMH 16
E
TMH 6
$D246^{6.50}$
$D703^{16.46}$
$S247^{6.54}$
$K707^{16.50}$
$E246^{6.53}$
$S184^{5.43}$
TMH 16

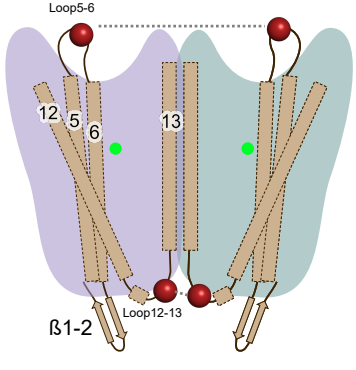

TmPPase:Ca^{2+}
(Model 1)

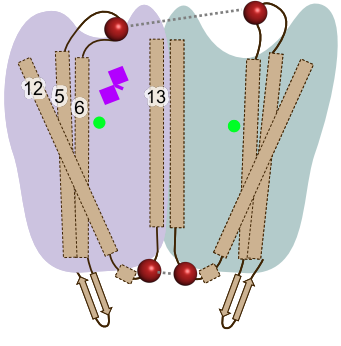

TmPPase:ETD:Ca^{2+}
(Model 2)

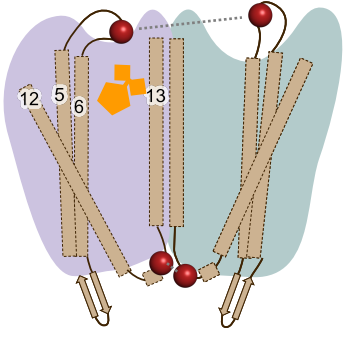

TmPPase:ZLD
(Model 3)

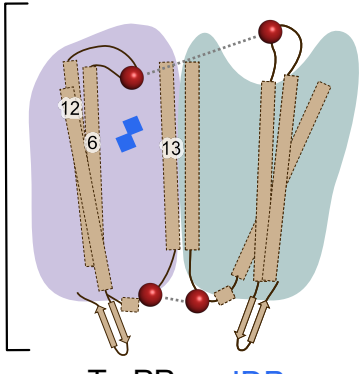

TmPPase:IDP
(Model 4)

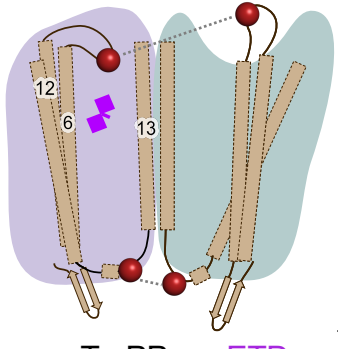

TmPPase:ETD
(Model 5)

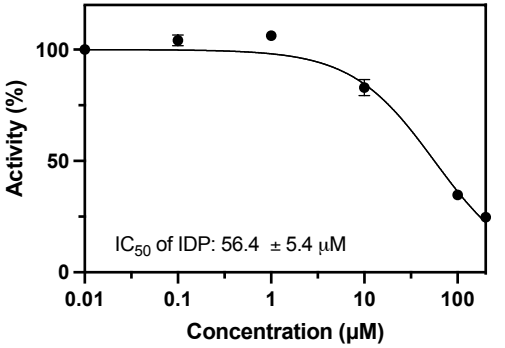
Activity (%)
100
50
0
0.01
0.1
1
10
100
Concentration (μM)
IC50 of IDP: 56.4 ± 5.4 μM

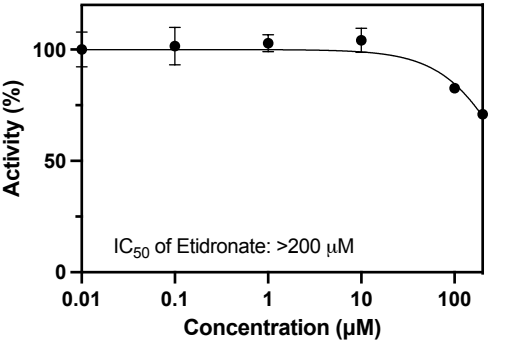
Activity (%)
100
50
0
0.01
0.1
1
10
100
Concentration (μM)
IC50 of Etidronate: >200 μM

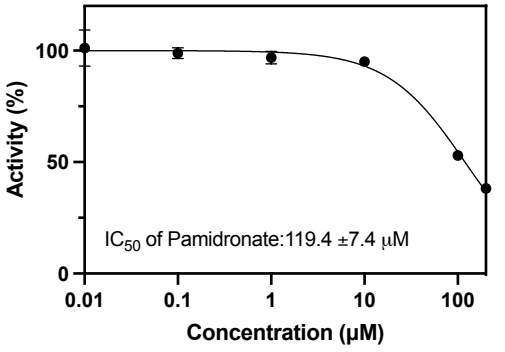
Activity (%)
100
50
0
0.01
0.1
1
10
100
Concentration (μM)
IC50 of Pamidronate:119.4 ±7.4 μM

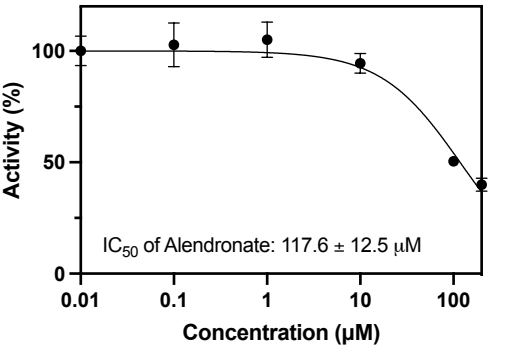
Activity (%)
100
50
0
0.01
0.1
1
10
100
Concentration (μM)
IC50 of Alendronate: 117.6 ± 12.5 μM

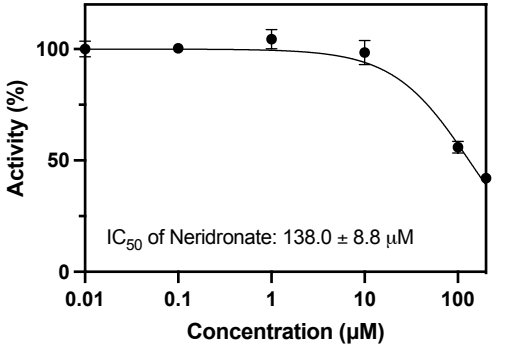
Activity (%)
100
50
0
0.01
0.1
1
10
100
Concentration (μM)
IC50 of Neridronate: 138.0 ± 8.8 μM

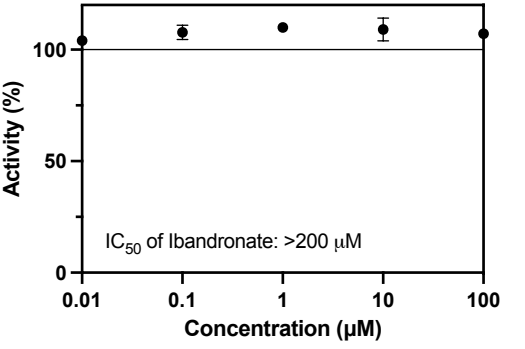
Activity (%)
100
50
0
0.01
0.1
1
10
100
Concentration (μM)
IC50 of Ibandronate: >200 μM

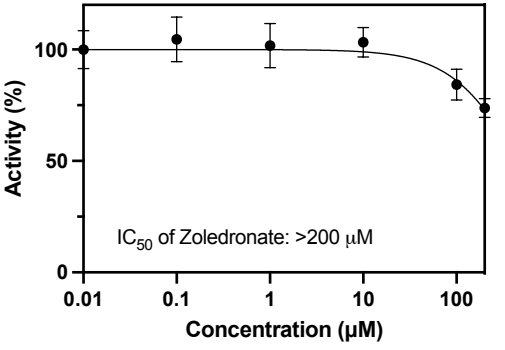
Activity (%)
100
50
0
0.01
0.1
1
10
100
Concentration (μM)
IC50 of Zoledronate: >200 μM

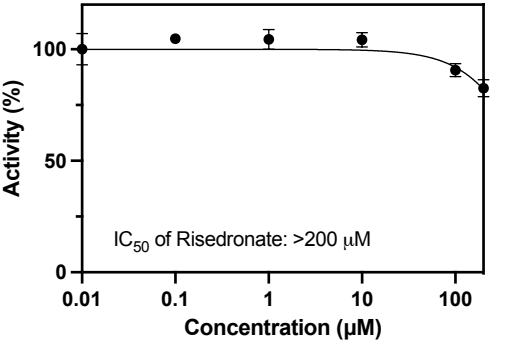
Activity (%)
100
50
0
0.01
0.1
1
10
100
Concentration (μM)
IC50 of Risedronate: >200 μM

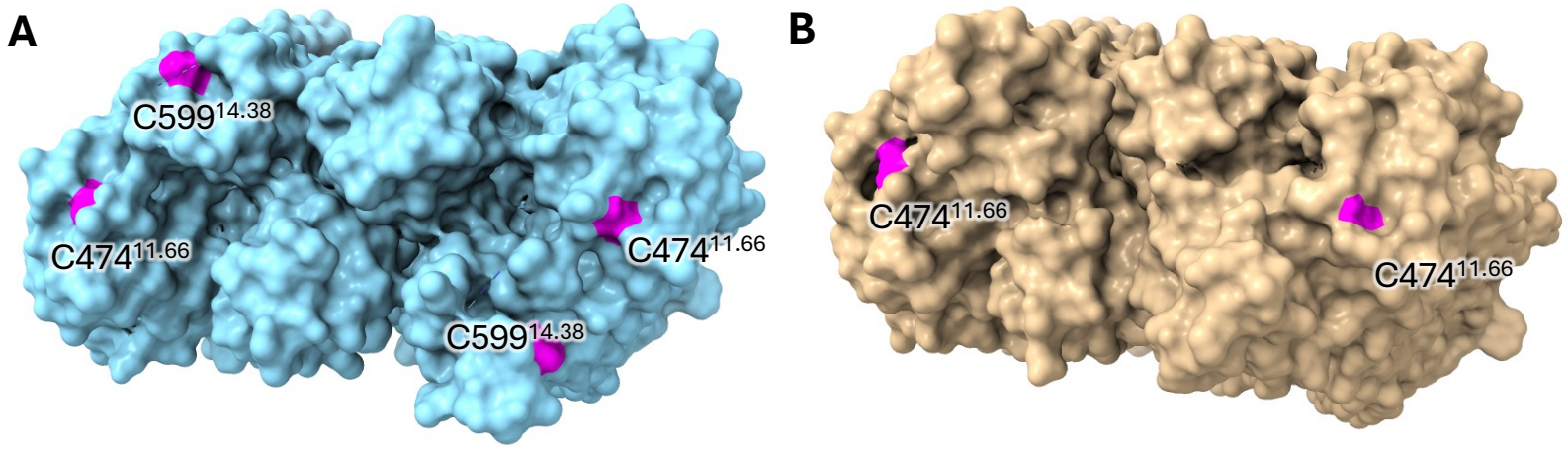
A
C599 14.38
C474 11.66
C474 11.66
C599 14.38
B
C474 11.66
C474 11.66

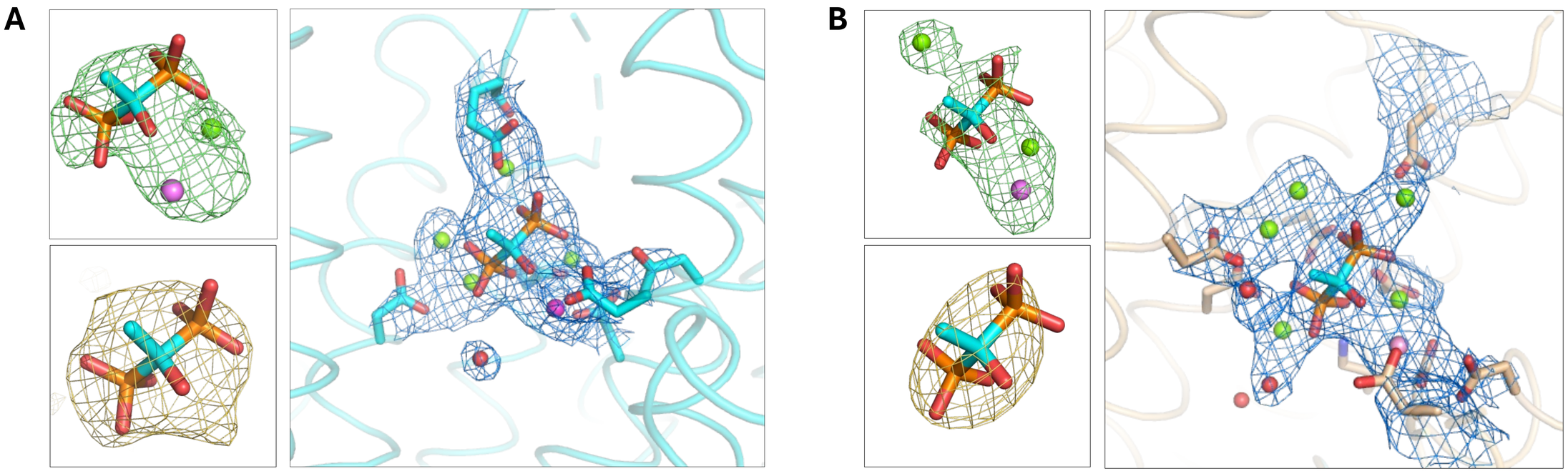
A
B

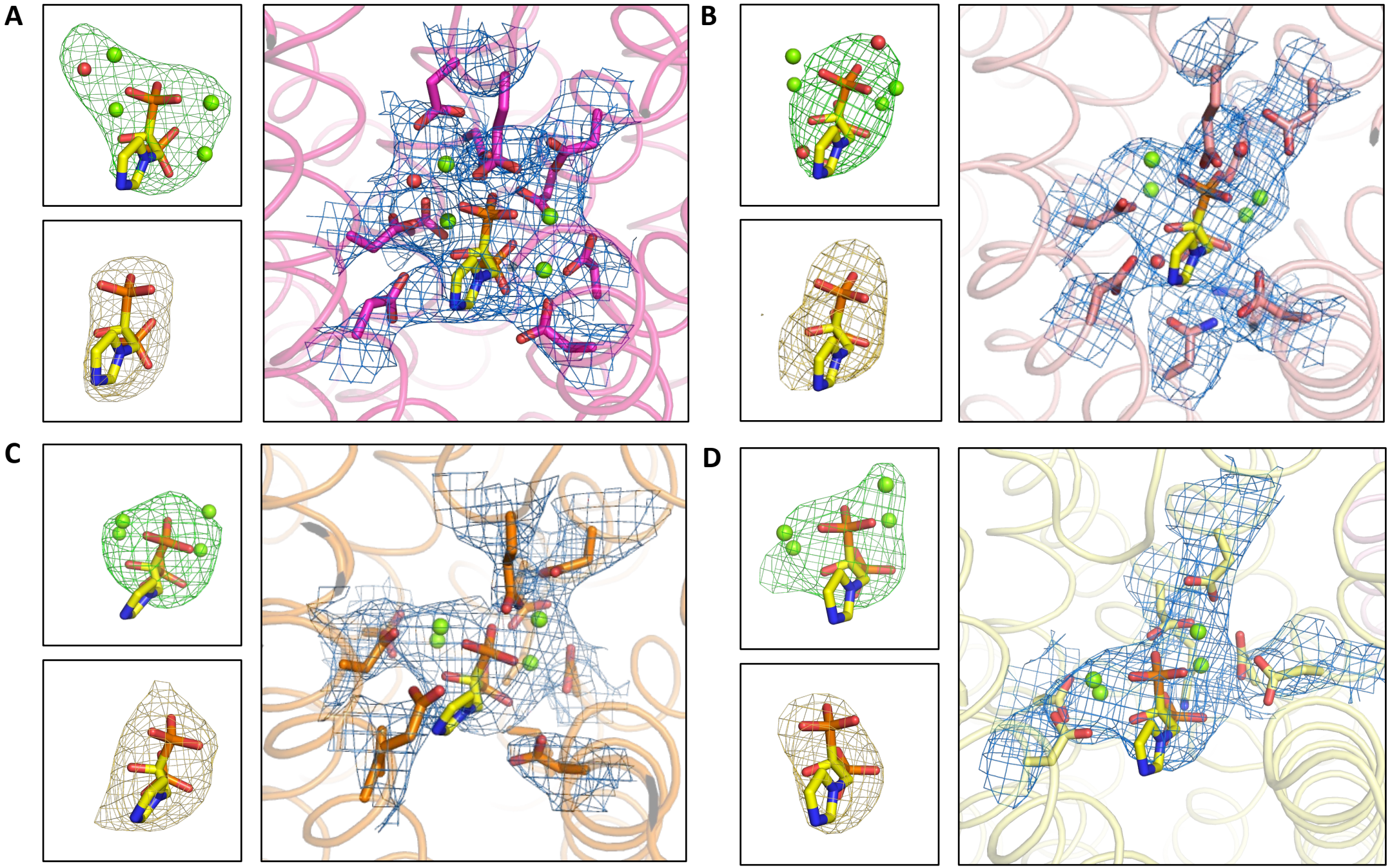
A
B
C
D

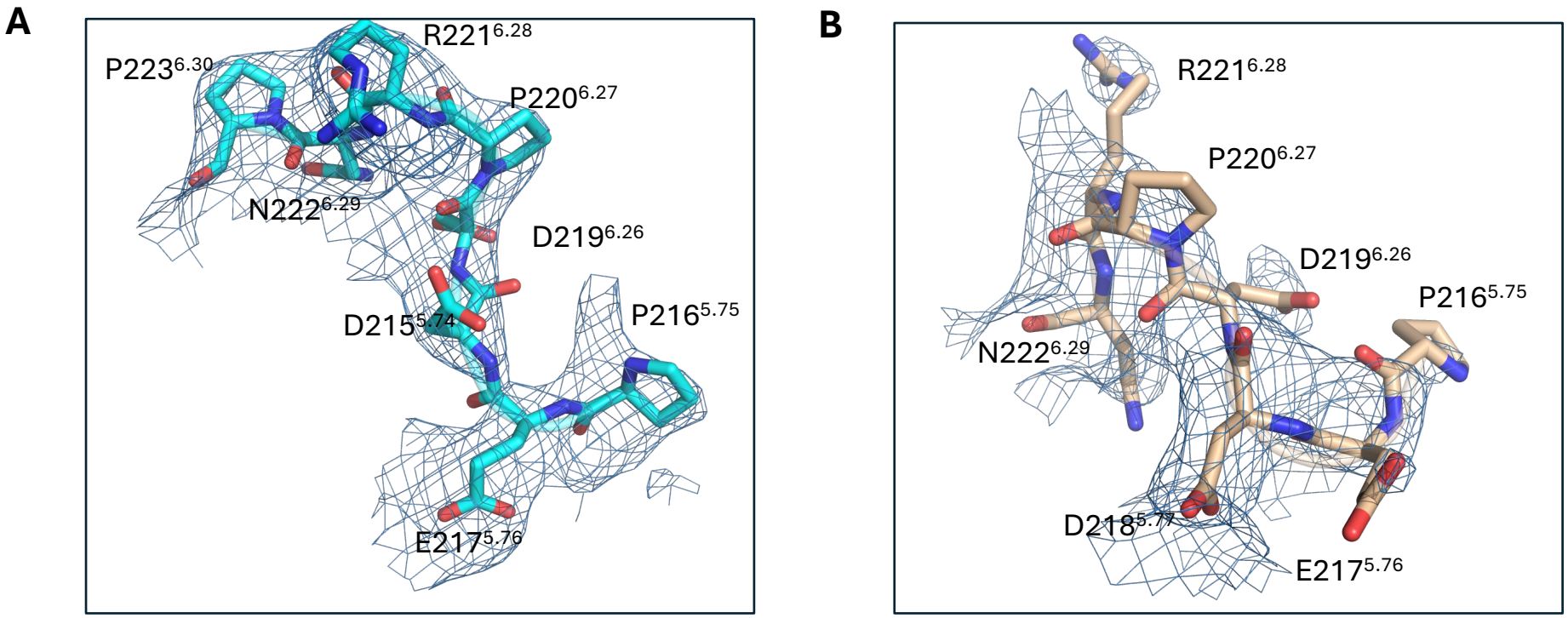
A
R221$^{6.28}$
P223$^{6.30}$
P220$^{6.27}$
N222$^{6.29}$
D219$^{6.26}$
D215$^{5.74}$
P216$^{5.75}$
E217$^{5.76}$
B
R221$^{6.28}$
P220$^{6.27}$
D219$^{6.26}$
P216$^{5.75}$
N222$^{6.29}$
D218$^{5.77}$
E217$^{5.76}$

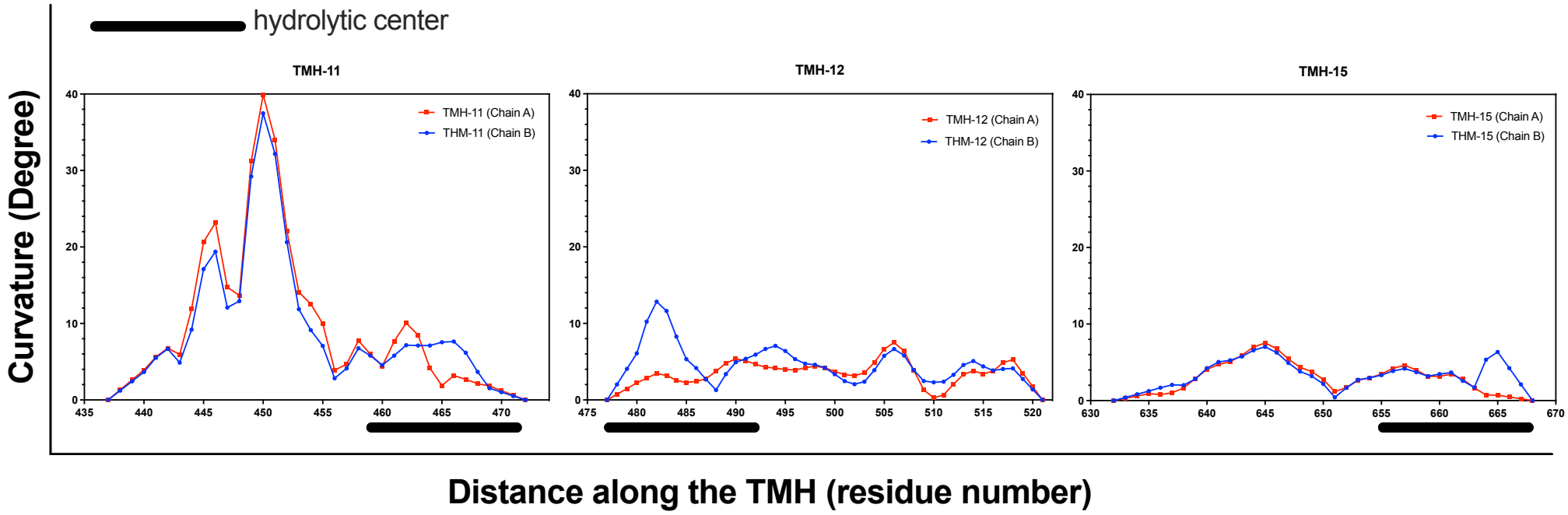
hydrolytic center
TMH-11
TMH-12
TMH-15
TMH-11 (Chain A)
THM-11 (Chain B)
TMH-12 (Chain A)
THM-12 (Chain B)
TMH-15 (Chain A)
THM-15 (Chain B)
Curvature (Degree)
Distance along the TMH (residue number)

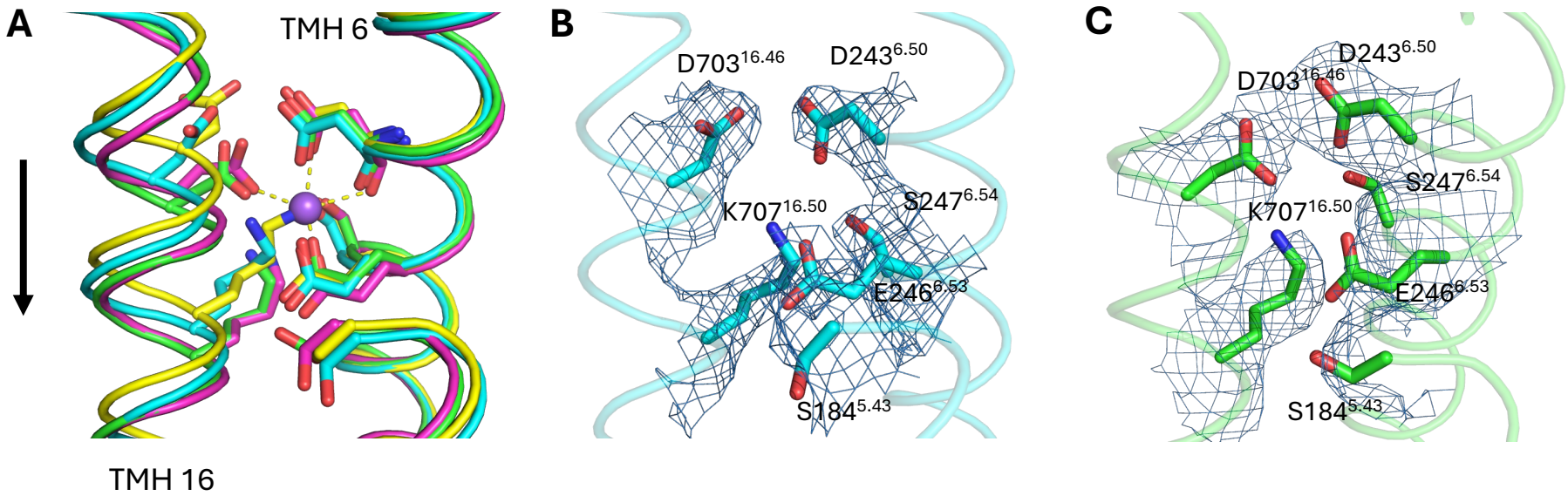
A
TMH 6
TMH 16
B
D703$^{16.46}$
D243$^{6.50}$
K707$^{16.50}$
S247$^{6.54}$
E246$^{6.53}$
S184$^{5.43}$
C
D243$^{6.50}$
D703$^{16.46}$
S247$^{6.54}$
K707$^{16.50}$
E246$^{6.53}$
S184$^{5.43}$

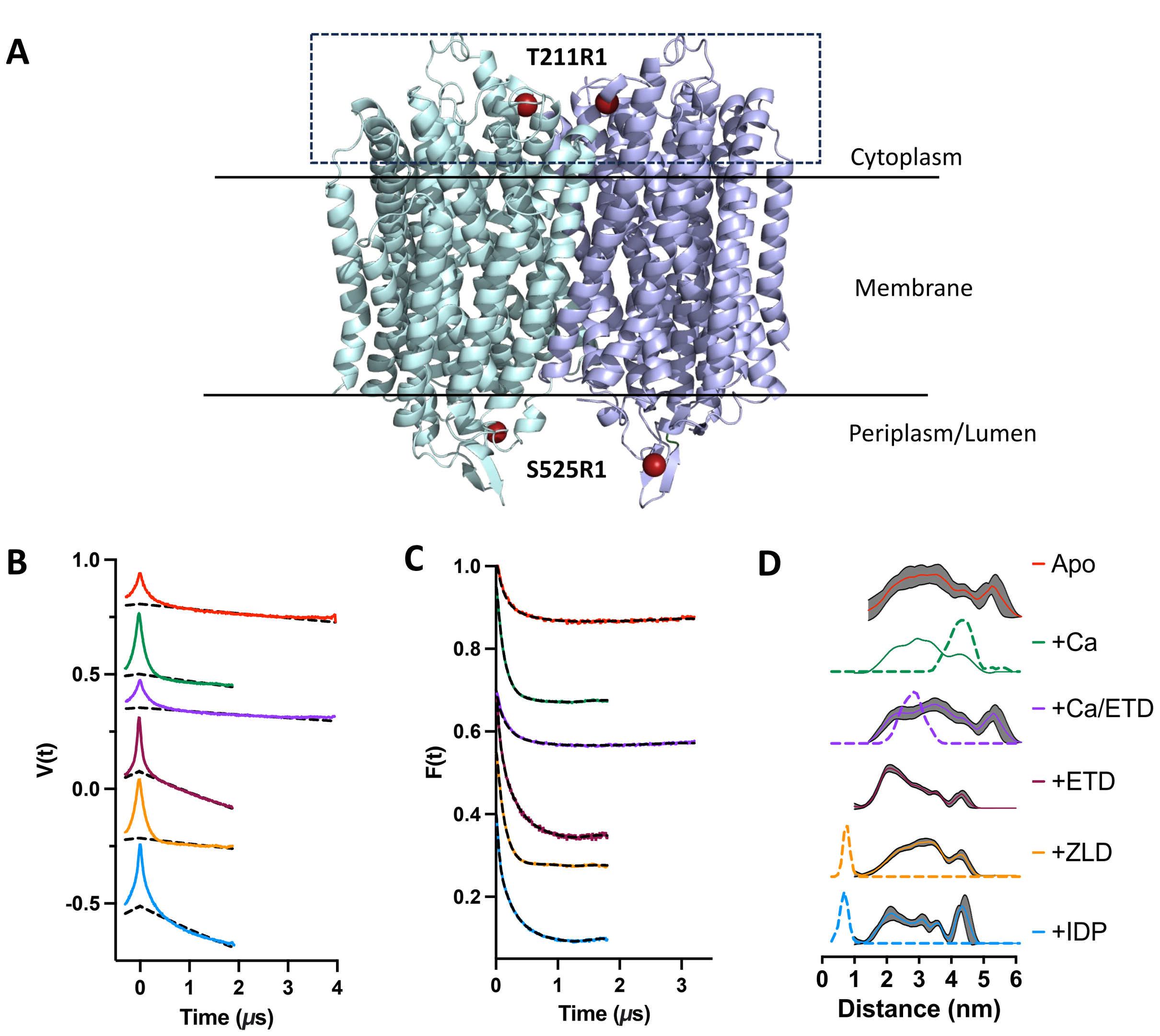
A
T211R1
Cytoplasm
Membrane
Periplasm/Lumen
S525R1
B
1.0
0.5
0.0
-0.5
V(t)
0
1
2
3
4
Time (μs)
C
1.0
0.8
0.6
0.4
0.2
F(t)
0
1
2
3
Time (μs)
D
Apo
+Ca
+Ca/ETD
+ETD
+ZLD
+IDP
0
1
2
3
4
5
6
Distance (nm)

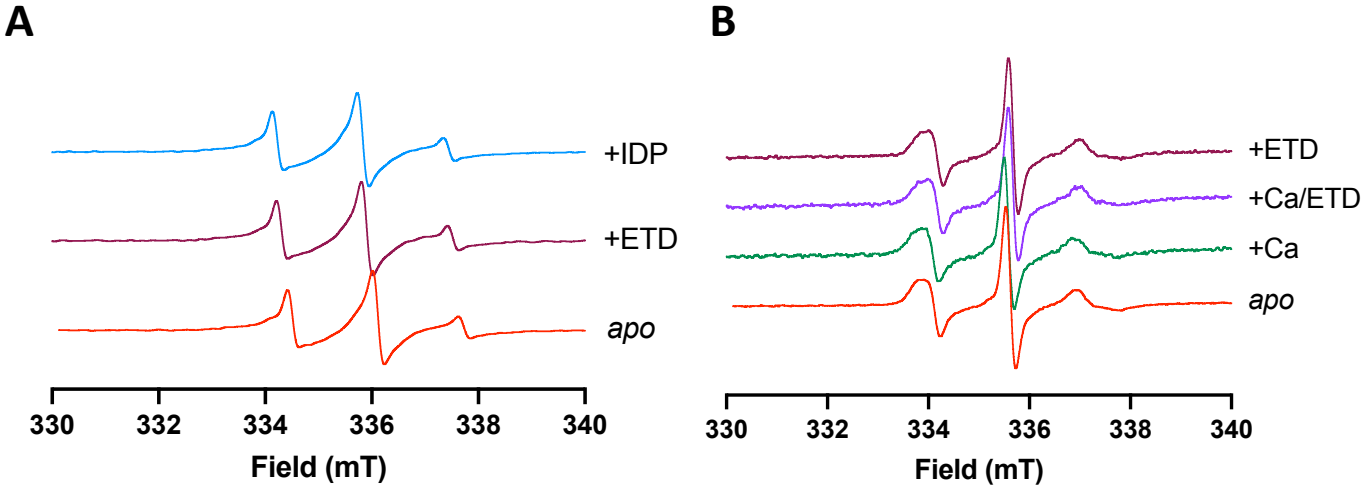
A
+IDP
+ETD
apo
330
332
334
336
338
340
Field (mT)
B
+ETD
+Ca/ETD
+Ca
apo
330
332
334
336
338
340
Field (mT)

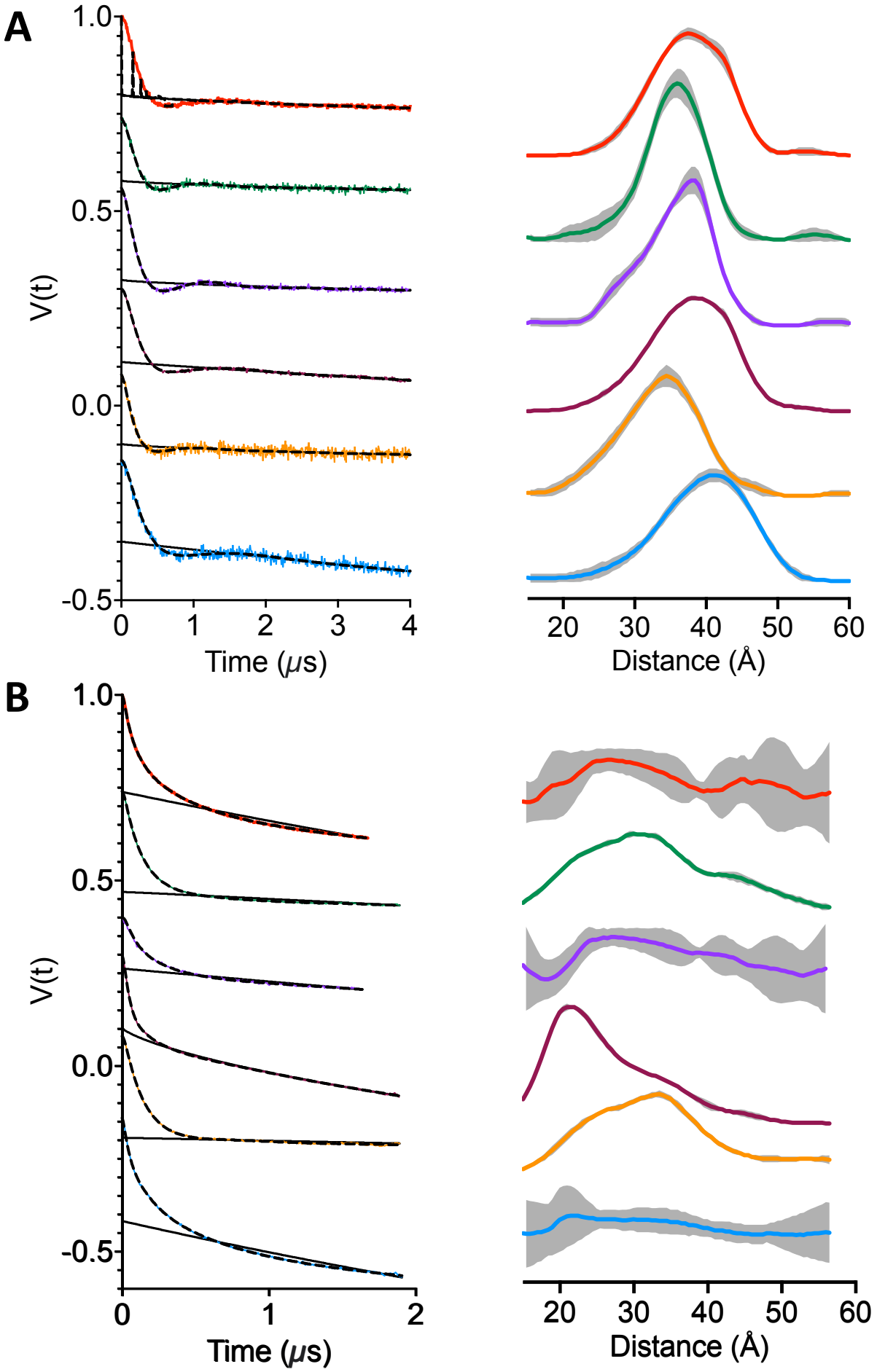
A
1.0
0.5
0.0
-0.5
V(t)
0
1
2
3
4
Time (μs)
20
30
40
50
60
Distance (Å)
B
1.0
0.5
0.0
-0.5
V(t)
0
1
2
Time (μs)
20
30
40
50
60
Distance (Å)